Infrared Observations of GRO J1655–40:
Constraints on the Black Hole Mass

Francis Thomas O'Donovan, B.Sc.

Thesis for the Degree of M.Sc.

submitted to

the National University of Ireland, Cork.

Research conducted at

the Department of Physics,

National University of Ireland, Cork.

Submission date: October 2003

Head of Department: Prof. S. Fahy

Research Supervisor: Dr. P. J. Callanan

Contents

Abstract

We present K_s– and J–band photometry of GRO J1655–40 during two epochs of observation, and determine the dereddened and absolute magnitudes of this star system. We derive a range of spectral types (F0–G2 III–IV) for the secondary star in GRO J1655–40, using our $J_0 - K_0$ colour estimate for this soft X–ray transient. We find the absolute magnitude of GRO J1655–40 to be similar to that of another long period soft X–ray transient.

The first high signal–to–noise K–band spectrum of a black hole X–ray transient system (GRO J1655–40) is presented. This is used to show that the quiescent contribution of the accretion disk in GRO J1655–40 to the total flux of the system in the K–band is negligible. We are therefore able to measure with certainty the binary inclination from the light curve of this stellar system, and place real bounds on the mass of the primary star in GRO J1655–40. GRO J1655–40 is also shown to have a similar spectrum to that of an F5–F7 III–IV star.

The ellipsoidal modulation observed in the K_s–band is modelled using ELC, to obtain an inclination of 64°–70° and a mass ratio of 2.5–6 for the system. These values concur with past results. The derived primary mass, $M_X = 6.8 \pm 0.7\,\mathrm{M_\odot}$, suggests that the compact object in GRO J1655–40 is a black hole.

An attempt is made to model the system in outburst, taking the ellipsoidal variability of the secondary star and the eclipse of a bright accretion disk into account. The resultant fit is poor, a consequence of the asymmetries of the disk and flickering in the K_s–band. The outburst light curve of GRO J1655–40 is shown to display an eclipse of the accretion disk, consistent with the high inclination of the system.

Acknowledgements

I would like to express my heartfelt gratitude for the support and advice of Dr. Paul Callanan. Throughout my undergraduate degree, Dr. Callanan encouraged my interest in astrophysics and provided me with the opportunity to gain experience in this field. His supervision of my M.Sc. has helped cement my interest and has given me valuable skills and knowledge. I am also indebted to him for his help in both selecting and securing a university place for my Ph.D. studies.

My thanks must also be given to the U.C.C. Physics Department. The academic staff have stimulated my mind for several years, while the technical and clerical staff have helped me with more practical matters. I must not forget my fellow students, especially Lisa Goggin, all of whom have helped me struggle through five years of Physics.

Thanks also to the present and former occupants of the Astrophysics Laboratory. Manuel Perez-Torres generously spent a lot of time explaining X–ray Binaries to me, in spite of the demands of his own Ph.D. John McCarthy and Peter Curran have both helped me in my research work and in the preparation of this document.

Finally, my sincere gratitude to my parents, Tom and Vera, and my sister, Bridget, who have supported and encouraged me throughout my entire education, and also to my dearest Gillian, who was very patient and understanding.

Chapter 1

Introduction

This thesis is concerned with the study of an X–ray binary star system, GRO J1655–40, which is thought to harbour a black hole. Before discussing this particular system in detail, a general introduction is given to black holes and X–ray binaries.

1.1 Black Holes

Possibly the most spectacular event in astrophysics is the death of a "massive" star, which is a star of mass greater than eight solar masses. After millions of years of phenomenal energy output, the star finally runs out of fuel. Most massive stars are then thought to form dense cores, called **compact objects**, and some eventually destroy themselves almost entirely. Such stars become a type of compact objects called **black holes**. This section introduces this exotic type of star and we will later explain the search for evidence of the existence of black holes.

Once a massive particle feels the gravitational attraction of a mass M, it requires a certain velocity, called the **escape velocity** (v_{esc}), to remove itself from that gravitational attraction. This velocity is given by the formula:

$$v_{esc} = \sqrt{\frac{2GM}{r}},\qquad(1.1)$$

where r is the distance between the masses, and G is the Gravitational constant.

At the end of the 18th Century, Michell and Laplace suggested the possibility of massive stars with $v_{esc} > c$. (Here, c is the speed of light in a vacuum.) These objects would always appear as black stars. With the development of Einstein's General Theory of Relativity, the modern picture of these "black holes" evolved: it is now thought that a black hole remnant is formed when a star of mass greater than ten solar masses ends its life cycle with a direct gravitational collapse. The matter remaining in the core of the star is totally devoid of nuclear fuel and hence is compressed by gravity until it converges to a singularity - a black hole.

The Schwarzschild Radius: the Size of the Black Hole

It is thought that each black hole is surrounded by an **event horizon**. This imaginary surface signifies the point of no return for any particle of mass or radiation: once the particle has passed beyond the event horizon, it is forever bound to the black hole. Not even light can escape, once it crosses this surface. Hence the compact object appears "black".

All the points on the event horizon are a certain distance from the black hole, called the **Schwarzschild radius** (R_{Sch}). At this radius, which is given by:

$$R_{Sch} = \frac{2GM}{c^2}, \tag{1.2}$$

the escape velocity equals the speed of light. This radius is often used to characterise the size of the black hole – these objects have no surface radius, being singularities.

How Can We Observe a Black Star in a Black Sky?

It is difficult to observe isolated black holes directly, as they emit very little radiation. However, the gravitational field caused by the mass of the black hole is more easily detected, especially if the black hole is gravitionally bound to a nearby star. When two stars are bound together like this by their mutual gravitational attraction, the pair is known as a **binary system**. We will later explore the specifics of binaries containing black holes, but we first briefly summarize various topics related to binary systems in general.

1.2 Binary Star Systems

The majority of "stars" seen in the night sky are in fact multiple–star systems, each of which contain two or more mutually-bound stars. Here we examine the characteristics of binary star systems.

1.2.1 Properties of a Binary System

The relative positions of the two component stars in a binary system to the observer is known as the **orbital phase**. Because the two stars in a binary system are orbiting about a common centre of gravity, the appearance of the system to an observer changes as the stars rotate, and the orbital phase of the system changes. (Figure 1.4 on page 8 shows various different phases for a type of binary system known as a **Cataclysmic Variable**). At **phase 0.0**, the observer sees the **secondary** (less massive) star in front of the **primary** star, and at **phase 0.5**, the secondary is behind. The primary star and secondary star are observed side by side at **phases 0.25** and **0.75**: these phases are known as the **quadratures**. (Phases 0.0 and 0.5 are similarly known as the **conjunctions**.) Note the time taken for the binary system to rotate through one complete cycle of phases is known as the **orbital period** (P).

The appearance of a binary system also depends on other properties of the system, such as:

- the **mass of the primary**, M_1, and the **mass of the secondary**, M_2 – the quantity $q = M_1/M_2$ is known as the **mass ratio**,

- the **angle of orbital inclination**, i, which is the angle between the observer and the normal to the orbital plane , and

- the **binary separation**, which is the distance between the two stars.

1.2.2 Ellipsoidal Variability of a Distorted Star

When the binary separation of a system is roughly comparable to the diameter of the star with the largest volume, the pair is called a **close binary system**.

The rotational and tidal forces acting on a star within a close binary system can cause a stretching of the star into a tear-drop shaped figure. In this thesis, most of the secondary stars in the systems we discuss are deformed in this way.

This deformation of the secondary star can modulate the brightness of the binary system. The apparent flux of the secondary varies as a function of orbital phase, because this flux is proportional to the projected surface area visible to the observer. As the binary system rotates, we see the projected surface area of the secondary star change (see, for example, Figure 1.4 on page 8). The amplitude of this variability depends primarily on the angle of inclination (i) and the mass ratio (q). It is largest for $i = 90°$.

For a given i, the projected surface area of the secondary star is at its maximum value at the quadratures. The flux from the secondary is therefore at its maximum value at phases 0.25 and 0.75. In a similar manner, the flux is at its minimum values at the conjunctions, when the secondary is observed end-on and the projected surface area is approximately circular.

Under normal circumstances (e.g., the star is in hydrostatic equilibrium), the local radiation flux on the surface of a star is proportional to the local surface gravity. This gives rise to **gravitational darkening**. At **inferior conjunction** of the secondary (phase 0.0), the tidally-undisturbed side of the secondary star faces the observer. All the points on the surface of the star are equidistant from the centre of the star, and hence have the same surface gravity and flux. However, at **superior conjunction** (phase 0.5), the star presents its distorted side, where the surface gravity is at its lowest, and hence the surface brightness is also at its lowest value. This results in a deeper minimum in the light curve of the secondary star at phase 0.5 than at phase 0.0.

In a binary system whose flux is dominated by that of the secondary star, the light curve of the system will show the same ellipsoidal variation as the secondary. An example of this **ellipsoidal variability**, also known as **double hump modulation**, is given in Figure 1.1 on the following page.

4
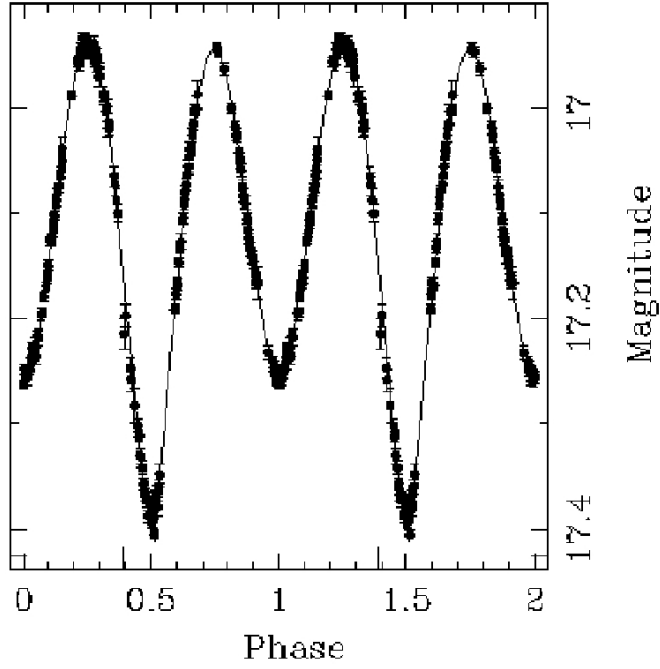
Figure 1.1: Model fit to the optical light curve of the X–ray binary GRO J1655–40, showing the characteristic ellipsoidal variability of a distorted secondary star. (Adapted from Orosz & Bailyn 1997.)

1.2.3 Eclipses in a Binary System

Another property of the light curve of a binary system is the presence or absence of **eclipses**. When the orbital inclination of a binary system is high enough, the component stars in the system will travel in front of each other as they orbit the centre of mass of the system. Since the closer star blocks the light of the further, the total flux from the system diminishes. These **eclipses** may be the most prominent features of the light curve of the binary. Of course, if the inclination is too low, no eclipses will occur. Therefore, the presence or absence of eclipses puts a limit on the value of the orbital inclination. Figure 1.2 on the next page shows a model of an eclipsing system with the resultant light curve.

5
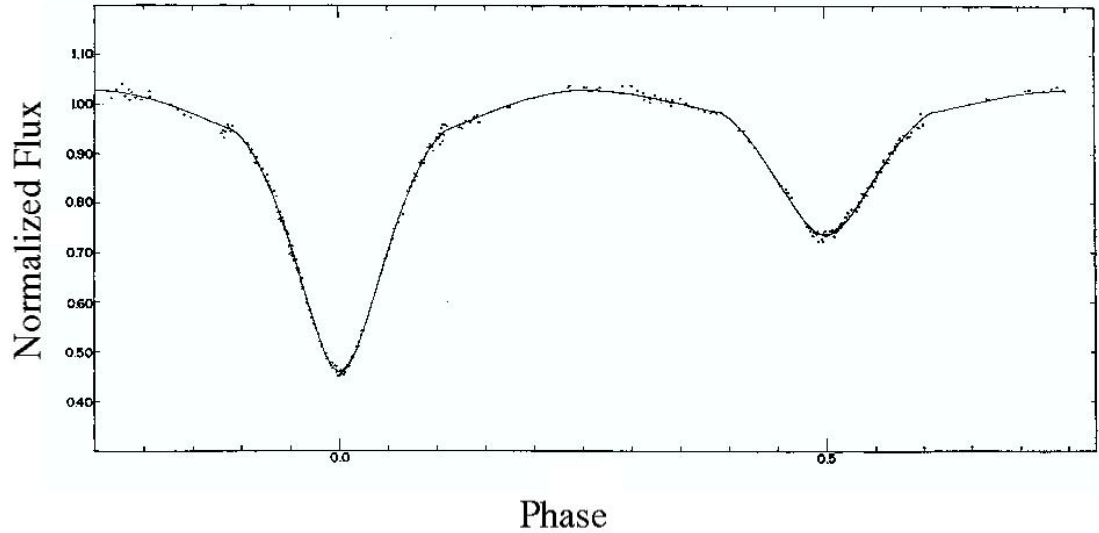
Figure 1.2: Observations of the eclipsing binary WR Cyg, overplotted with a theoretical light curve. (Adapted from Wilson & Devinney 1971.)

1.2.4 Accretion onto the Primary

An important effect of the deformation of the secondary star in a close binary is the possible transfer of mass from one star to the other. This process is known as **accretion** or **mass transfer**. Whether it occurs depends on the sizes and separation of the component stars, as we now explain.

Accretion and the Roche Lobes

During the 19th century, the French mathematician Edouard Roche studied the interactions of planetary satellites. His work has been applied to binary systems to develop a theoretical model for accretion.

By studying the gravitational interaction between two objects, Roche developed a series of curves representing equipotential surfaces surrounding the pair (see Figure 1.3 on the following page). The shape and size of these curves are determined by the mass ratio of the two objects and their separation. The most important curves are the two so-called **Roche lobes**, the "figure of 8" shaped surface.

6
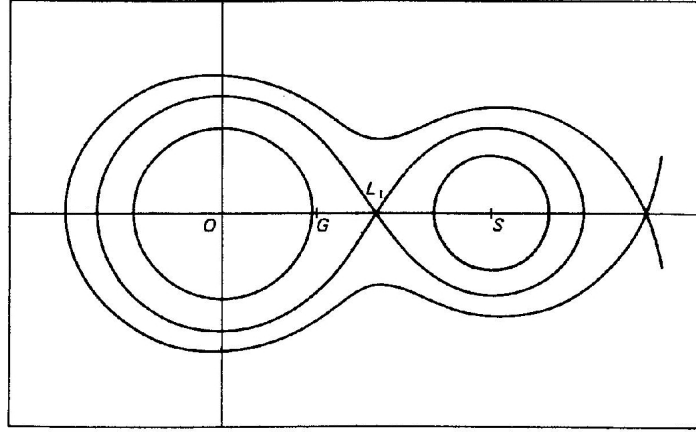
Figure 1.3: Example of the Roche equipotentials for a binary system. The centre, O, of the primary star is marked, as is the centre, S, of the secondary star. Also marked are the Lagrangian point, L_1, and the centre of mass, G, of the system. The mass ratio is given as $q = 2$. (Adapted from Pringle 1985.)

As the **companion** (secondary) star evolves, its size increases and it may expand to fill its Roche lobe. Some of the matter of that star may lie on or even outside this lobe, and some of this matter will be attracted towards the primary. The gas will flow towards the primary through the **inner Lagrangian point** (L_1), which is the intersection of the Roche lobes. This process is known as **Roche lobe overflow accretion**. Such a binary system is known as a **semi-detached binary**, if the radius of the primary star is less than its Roche lobe radius. If the companion star of a binary system does not fill its Roche lobe, then the stellar matter is bound and no mass transfer to the primary occurs by Roche lobe accretion. In some such systems, mass transfer can still occur via a **stellar wind**, a stream of gas particles flowing out from the star, similar to the solar wind. In this thesis, however, we are mainly concerned with Roche lobe overflow accretion.

The characteristics of binary systems that we have outlined are common to all binaries – we now detail the specifics of the type of binary systems known as X–ray binaries.

1.3 X–ray Binaries
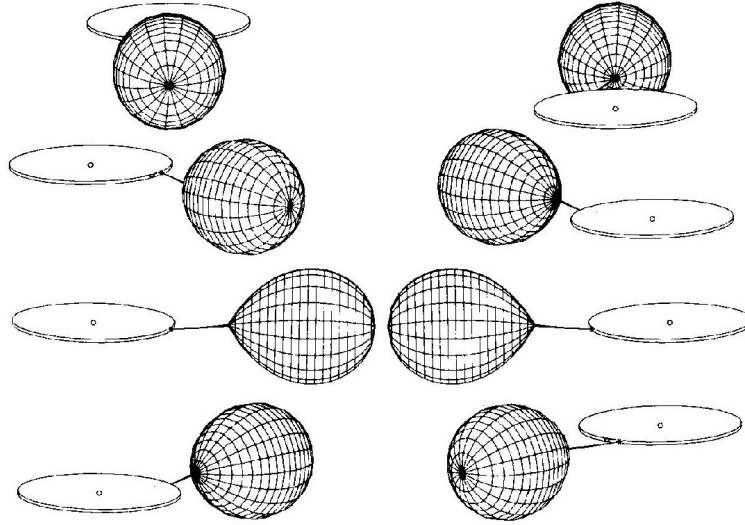
Figure 1.4: The observed relative positions of the component stars of a cataclysmic variable as a function of orbital phase, beginning with phase 0.0. The phase difference between images, going from top to bottom, is 0.125. (Adapted from Pringle & Wade 1985.)

Many semi-detached binary systems have a compact primary star and a nondegenerate secondary. (For the remainder of this discussion, such a binary system will be assumed unless otherwise stated.) This compact object may be a white dwarf, neutron star or black hole.

When the primary star of such a system is an accreting white dwarf, the system is a **cataclysmic variable** (see Figure 1.4 for an example): these variables are divided into such categories as the brighter **classical novae**, the fainter **dwarf novae** and the **novalike objects**. The radiation emitted by these systems is chiefly in the optical and ultraviolet regions of the electromagnetic spectrum.

When the primary in a close binary system is a neutron star or black hole, the binary is called an **X–ray binary**. X–ray binaries take their name from the fact that the majority of the energy radiated from the bright systems during phases of high accretion is in the form of X–rays (with energies 0.1–100 keV). (We denote

the mass of this X–ray emitting object by M_X.) In an X–ray binary, the radius of the compact primary will always be less than its Roche lobe radius, hence these systems are always semi-detached.

In 1962, Giacconi et al. discovered the first known X–ray emitting cosmic object in the constellation of Scorpius (Giacconi et al. 1962). The source, christened Sco X–1, was later shown to be a binary system, and is usually the brightest X–ray binary in the sky. The first confirmed X–ray binary, however, was Cyg X–1 (Webster & Murdin 1972; Bolton 1972). Since this observation, approximately 300 X–ray binaries have been identified (Liu, van Paradijs, & van den Heuvel 2000, Liu, van Paradijs, & van den Heuvel 2001).

Once the first X–ray binaries had been identified optically, their distances and hence their intrinsic X–ray luminosities were determined. Some of the luminosities calculated were of the order of 10^{31} W, which is approximately 10^5 $L_\odot$ (where $L_\odot$ is the luminosity of the Sun[1]). Shklovsky (1967) suggested that this unusually high luminosity of X–ray binaries such as Sco X–1 could be accounted for if they were mass-exchanging binaries with a neutron star component. This was the first realisation that accretion was an important power source. Much of the energy radiated by these systems comes from a disk of gas around the primary star – the **accretion disk**.

1.3.1 The Accretion Disk

In a binary where accretion is taking place, if there is a continual stream of particles flowing from the the secondary star to the primary, the gas forms a disk, known as the **accretion disk**. The rotation of the secondary star imparts angular momentum to the matter flowing into this disk. Viscous processes redistribute the angular momentum amongst the gas particles, which causes the in–falling of some of the particles onto the primary. The in–falling gas is heated until it forms a highly ionized plasma, with highest temperatures closest to the primary.

An accretion disk is very efficient at converting the gravitational potential

---

[1] $1\,L_\odot = 3.826 \times 10^{26}\,$W

energy of the transferred matter into radiation. For example, about 20% (for a neutron star primary) or 30% (for a black hole primary) of the rest energy of the accreted gas may be emitted as radiation. The accretion results in a luminosity of the primary given by:

$$L = \frac{GM_X \dot{m}}{R_X},$$ (1.3)

where R_X is the radius of the primary star, and $\dot{m}$ is the rate of mass transfer from the secondary star onto the primary star. (Note that this formula does not strictly apply to black holes, as it assume a primary star with a hard surface.) There exists an upper limit for L, called the **Eddington Limit (L_E)**, above which the outer parts of the star cannot remain in hydrostatic equilibrium. Above L_E, the process of accretion is halted due to the radiative pressure from the star, and in fact mass loss from the primary may occur.

Using Equation 1.3, and assuming a solar mass primary, we see that the high luminosities mentioned on page 9 can be generated by an accretion rate of only $10^{-8}\,\mathrm{M_\odot\,yr^{-1}}$ (e.g., Fabian 1985), reflecting the aforementioned efficiency of accretion as a power source. (Here $\mathrm{M_\odot}$ is the mass of the Sun[2].)

Reprocessing of Radiation

An important effect of accretion in the case of X–ray binaries is a process called **X–ray reprocessing** or **X–ray heating**. The X–ray radiation emitted by the accreting material interacts with the matter in the accretion disk, in the secondary star or surrounding the binary system. This interaction converts some of the emission into optical and infrared (IR) radiation. This X–ray heating can affect the appearance of the disk and the secondary star, as we will later see.

1.3.2   Categorisation of X–ray Binaries

X–ray binaries are generally categorized by the mass of the secondary star, which is classified as either a high mass or a low mass star. The two corresponding categories are the **High-Mass X–ray Binaries (HMXBs)** and the **Low-Mass**

---

[2] $1\,\mathrm{M_\odot} = 1.99 \times 10^{30}\,\mathrm{kg}$

X–ray Binaries (LMXBs). As well as mass distinctions, X–ray binary systems can be divided into two categories on the basis of the variability of their luminosity: X–ray binaries which display transient high-energy emissions are known as **transient X–ray binaries**, while those with persistently bright behaviour are known as **persistent X–ray binaries**. We first consider the two mass–related categories.

1.3.3   High-Mass X–ray Binaries (HMXBs)

High-Mass X–ray Binaries contain companion stars with masses of $\gtrsim 10 \, \mathrm{M_\odot}$. These stars are O or B giants or supergiants, with temperatures of roughly 20,000 K, and have survived the supernova explosion of their evolved companion. The compact object in the majority of HMXBs (67 of the 70 known) is a pulsating neutron star. The other three HMXBs are thought to harbour black holes, and are persistent sources.

HMXBs tend to have large binary separations (due to the giant size of the secondary) and therefore long orbital periods. The periods range from 4.8 hours to 188 days (van Paradijs 1995), with the eccentricity of the orbit increasing with the period.

Despite this large separation, the size of the secondary star may permit mass transfer onto the primary via a stellar wind or even Roche lobe overflow accretion. Mass loss rates of between 10^{-6} and $10^{-10} \, \mathrm{M_\odot} \, \mathrm{yr}^{-1}$ can be achieved by stellar winds (White, Nagase, & Parmar 1995), and the compact object captures a small fraction of this mass.

One of the main characteristic of a typical HMXB is the observation of **outbursts**, or high brightness states, at regular intervals, caused by the interaction of the neutron star with the stellar wind surrounding the secondary star. The companion dominates the optical and infrared luminosity of the system, but X–ray reprocessing and the presence of an accretion disk do modulate this luminosity.

1.3.4   Low-Mass X–ray Binaries (LMXBs)

The secondary star of an LMXB has a mass of $\lesssim 1\,\mathrm{M_\odot}$ and is generally a K or M dwarf star. The number of observed LMXBs is greater than that of observed HMXBs: Tanaka & Lewin (1995) estimate the number of known LMXBs to be about 125, with 39 observed X–ray transient LMXBs. Of these 125, 17 LMXBs are thought to contain black holes, with 14 in X–ray transient systems.

The size of the companion star determines the binary separation, as a small companion requires a small separation in order for mass transfer to occur. The orbital period of the binary system is therefore affected by the nature of the companion. Systems with dwarf companions have periods of the order of hours, whereas binaries containing evolved companion stars have orbital periods of the order of days. The periods of known LMXBs range from 11.4 minutes to 16.6 days (van Paradijs 1995). The shortest periods are possible only because of the low mass of the companion star.

The category of Low Mass X–ray Binaries can be divided into two sub-categories:

- The systems which are continually bright are denoted **persistent LMXBs**, and almost all of these contain neutron stars. The accretion disk is brighter than the secondary star for almost all of the persistent LMXBs. Therefore the optical spectrum is that of the hot disk with emission lines superimposed (see, e.g., Shahbaz et al. 1996) and appears blue. The spectrum of the secondary star is only observable for those persistent LMXBs with long orbital periods.

- The LMXBs which exhibit transient behaviour are known as **soft X–ray transients (SXTs)**. Most SXTs ($\geq 70\%$) are thought to contain black holes. One reason these transients are studied is that it is possible to observe the secondary star during the long periods of quiescence. Another benefit is that the large range in luminosities of these objects allows accretion models to be tested over a range of mass accretion rates for a given system. Neither of these are possible with the persistently bright sources.

It is to these transient LMXBs that we now direct our attention.

1.3.5 Soft X–ray Transients (SXTs)

Harries et al. (1967) discovered the first **Soft X–ray Transient**, Cen X–2, when they detected a very bright X–ray source during rocket flights. At its peak, this bright source outshone Sco X–1, but it later diminished. Transients like Cen X–2 were first studied in the 2–10 keV range, where a soft component in their spectra can be seen. This led to their designation as soft X–ray transients, even though they often exhibit very hard spectra at higher energies.

All soft X–ray transients display the two state behaviour of Cen X–2. The low accretion and low brightness state, or **quiescence**, can last for months to decades. The **outburst** state occurs when the accretion rate onto the compact object is dramatically increased (in some cases caused most likely by an instability in the accretion disk), with a corresponding increase in luminosity. These outbursts last only briefly, but the outbursts of many, if not all, transients are recurrent. The luminosity of a soft X–ray transient typically increases by a factor of 10^3–10^4 as the system passes from its quiescent phase into outburst, and the outburst luminosity is usually between 10^{30} W and 10^{32} W (Tanaka & Lewin 1995).

Since the discovery of Cen X-2, approximately 23 SXTs have been observed, of which only 25% contain neutron stars. SXTs are now being discovered at a rate of 1 or 2 per year. The prototype SXT is A0620-00 (Nova Mon 1975), noted by Elvis et al. (1975) to be the brightest extrasolar X–ray source for several months. Indeed, when in outburst, SXTs are among the brightest sources in the X–ray, but they may be undetectable in this region of the spectrum during quiescence.

Because of the large change in the brightness of SXTs from quiescence to outburst, and because both SXTs and dwarf novae (see page 8) have variable accretion rates, SXTs are also known by the less accurate term **X–ray novae (XRNe)**. The disk instability models applied to dwarf novae have been adapted for SXTs (see, e.g., Meyer-Hofmeister & Meyer 2000), but the effect of the X–ray irradiation of the disk and the secondary must also be taken into account.

Nevertheless, these models should hold for SXTs during quiescence, where there is negligible X–ray heating of the secondary and the disk.

Because all LMXBs vary to some extent, some criteria must be applied to determine whether a LMXB is a persistent or transient source. An LMXB is generally denoted as an SXT if the following holds (Tanaka & Shibazaki 1996):

1. The X–ray flux from the binary has rapidly increased from its quiescent value by more than two orders of magnitude within only a few days.

2. The flux has then been reduced (exponentially) to its quiescent value over a period of about 10–100 days.

3. If the outburst has recurred, the time scale of the outburst was smaller than the quiescent stage (typically decades: Hynes et al. 1998).

4. The outburst has not recurred with a regular period.

1.3.6 SXTs in Outburst

During X–ray outburst, the X–ray luminosity, L_X, of an SXT increases until it reaches the Eddington limit (see 1.3.1 on page 10). Outbursts at optical wavelengths are also observed.

In many SXTs the solid angle of the secondary, viewed from the compact star, is small, and so the reprocessing of X–rays takes place mainly in the accretion disk, rather than the secondary. A typical accretion disk in a transient LMXB during outburst is illuminated by approximately one quarter of the flux from the compact star, or approximately 10^{30} W (van Paradijs & McClintock 1995). The resultant intense heating of the disk causes the luminosity of the disk to be far greater than that of the faint K or M dwarf secondary, which is typically 10^{26} W. The change in the optical brightness of the SXT is therefore due to the changing visibility of the accretion disk. The light curve has one maximum and minimum per orbital cycle, and the minimum occurs when the secondary is closest to the observer.

This dominance of the disk contribution to the optical brightness means that ellipsoidal variations are only observed during the quiescent states of transient LMXBs. During quiescence, the X–rays are mostly absent and the disk and secondary are not significantly heated.

1.3.7   The Quiescent Period of an SXT

During quiescence, the weak emissions from the dwarf secondary should dominate the optical and infrared. Hence, the ellipsoidal variability due to the secondary is observable directly during this state.

The disk is hotter than the secondary, however, and therefore it contributes more at shorter wavelengths. The disk also contributes a constant flux offset and possible random flickering. This aperiodic flickering may cause the light curve to change from one observation to the next (see, e.g., Chevalier et al. 1989), and the veiling of the secondary by the accretion disk reduces the fractional amplitude of the ellipsoidal variability.

During quiescence, mass transfer continues, suggesting the Roche lobe of the secondary remains filled. The quiescent X–ray luminosity, L_X, is of the order of 10^{23}–10^{26} W, and is usually much less than the optical luminosity.

1.3.8   SXTs and Black Holes

Soft X–ray transients have proved very important in the study of black holes. It is difficult to distinguish between an X–ray binary containing a neutron star and one harbouring a black hole. One possible criterion for differentiating between neutron stars and black holes is the mass of the star: Rhoades & Ruffini (1974) and Chitre & Hartle (1976) showed that the maximum mass of a neutron star is approximately $3\,\mathrm{M}_\odot$. This limit is based on certain assumptions, such as that General Relativity is the correct theory of gravity, and that causality holds inside the neutron star (i.e., sound cannot travel faster than light). Nevertheless, compact objects with masses greater than this limit are generally considered to be black holes. This star is then referred to as a **black hole candidate (BHC)**.

Table 1.1: Two of the Best Studied SXTs with BHC Primaries

System	$f(M_X)/\mathrm{M_\odot}$	$M_X/\mathrm{M_\odot}$	P^a
V404 Cyg^b	6.26 ± 0.31	8–12	$6^{\mathrm{d}}473 \pm 0^{\mathrm{d}}001$
A0620-00^c	3.18 ± 0.16	7–15	$7^{\mathrm{h}}75234 \pm 0^{\mathrm{h}}0010$

^{a}The orbital period of the binary.
^{b}Casares, Charles, & Naylor (1992)
^{c}McClintock & Remillard (1986)

Webster & Murdin (1972) and Bolton (1972) discovered the first BHC in the binary system Cyg X-1, which has a primary with a mass of $\gtrsim 3\,\mathrm{M_\odot}$. Since then, the increase in the number of strong Galactic BHCs is in part due to the discovery of SXTs: a remarkably high fraction[3] of the SXTs currently known are thought to harbour black holes (van Paradijs 1998). Table 1.1 lists two of the best known soft X–ray transients containing black hole candidates, together with their system properties.

The detection of a high fraction of SXTs containing BHCs is due to the lower accretion rates for systems with black holes, and to the extended periods of quiescence in SXTs, as we now explain:

- The accretion rate for an X–ray binary generally decreases as the mass of the primary increases and the secondary star evolves (Casares 2001). Therefore, binaries with the more massive black holes are more likely to be transient sources than those with neutron stars, as their accretion rates are more likely to be below the critical accretion rate[4] (King, Kolb, & Burderi 1996). This also accounts for why most SXTs have highly evolved secondaries.

- Also, the extended periods of quiescence, absent from persistent sources, enable accurate determination of the component masses of the binaries. It is therefore more likely that compelling evidence of a black hole would be found in an SXT rather than in another persistently bright X–ray binary with similar system properties.

[3]A higher fraction than any other class of Galactic X–ray sources.
[4]A system will be transient or persistent depending on its accretion rate. The **critical accretion rate** is the rate above which the system will be persistent.

Many of the X–ray peculiarities of Cyg X–1, the first BHC, were originally assumed to indicate the black hole nature of a source (Tanaka & Lewin 1995). These characteristics were :

1. an ultrasoft X–ray spectrum,

2. millisecond X–ray flickering,

3. a high, soft state and a low hard X–ray state, and

4. a hard X–ray tail.

However, neutron star systems, such as Cir X–1 and X0331+53, have also been shown to display these properties. Although the presence of properties similar to these characteristics of Cyg X–1 are indeed suggestive of a black hole nature, the most persuasive determination is the calculation of the mass of the collapsed star. A lower limit to this mass can be made by calculating the **mass function** of the star.

1.3.9   The Mass Function

Applying Kepler's Laws to the binary system, it is possible to derive the following result:

$$\frac{M_X^3 \sin^3 i}{(M_X + M_2)^2} = \frac{P K_2^3}{2\pi G},$$

(1.4)

where K_2 is the **radial velocity** semi-amplitude[5] of the secondary star. The right hand side of Equation 1.4 is defined to be the **mass function of the primary star,** $f(M_X)$, and is a lower limit approximation of the mass of the compact object, since the left hand side of this equation is always $\leq M_X$. A similar definition can be made for the mass function of the companion $f(M_2)$, which gives a lower limit for the mass of the companion.

Since the mass function of the primary star sets a lower limit for the mass of the star, finding a primary whose mass function is above the limit of Rhoades

---

[5]The **radial velocity** of a star is the velocity of the star along the line of sight of the observer. The semi-amplitude of the radial velocity is normally measured by calculating the Doppler shift of absorption features in the spectrum of the secondary star.

& Ruffini (1974) suggests that the star is a black hole. One of the highest mass functions yet measured is that of XTE J1555–564 ($6.86 \pm 0.71 \, \mathrm{M_\odot}$: Orosz et al. 2002), well above the neutron star limit.

1.3.10   Determining the Mass of the Primary

Rather than setting a limit to the mass of the primary using the mass function, if we can constrain the mass of the secondary (say from consideration of its spectral type), we can calculate M_X from the mass ratio q. But first we must contrain q and i.

The simplest method to calculate q is to determine the velocity curve for both the primary and secondary star. Unfortunately, this is not feasible for X–ray binaries with black hole primaries (such as GRO J1655–40) because there is no direct method for observing the radial velocity v_r of the black hole.

An alternative method to determine the mass ratio is to measure the rotational broadening of the spectral lines of the secondary star (e.g., van Paradijs & McClintock 1995). This broadening is caused by the varying radial velocity across the stellar disk, and the resultant relative Doppler shift of the light from different parts of the star (see, e.g., Gray 1992 for details.)

Finally, the method we employed to determine the mass ratio for GRO J1655–40 was to use the ellipsoidal variability of the companion star to constrain both the mass ratio and the inclination[6]. The accuracy of this method is reduced by the presence of a luminous accretion disk or asymmetries on the surface of the star (e.g. **starspots**).

The light curve of an SXT during quiescence is normally that of the ellipsoidal variability of the secondary star. This can be modelled to constrain the orbital inclination and mass ratio of the system. However, if there is significant light from

---

[6] The presence (or absence) of eclipses in the light curve of a binary system immediately implies that the orbital inclination is close to (or far from) $90°$. An improved estimation of i can be calculated from the duration of the eclipses.

a luminous accretion disk present, this will affect the light curve. The luminous disk will compete with the secondary star, and distort the ellipsoidal variability of the system, reducing the accuracy of the derived mass ratio. This contamination may be reduced by the use of infrared observations (which we explain later), but this may not eliminate the disk contribution entirely.

If the accretion disk contribution is ignored, this may lead to an underestimate of the mass ratio, and hence the derived masses of the component stars (e.g., Shahbaz, Bandyopadhyay, & Charles 1999). Therefore, in order to obtain true estimates of the masses, we must first determine the contribution of the disk.

For this thesis, spectroscopy was used to determine the contribution of the accretion disk in a binary system to the overall K–band flux of the system. The spectrum of a main-sequence secondary star in a binary system displays absorption features, whereas the accretion disk exhibits emission features. The spectrum of the binary system therefore depends, partially at least, on what fraction of the flux of the system originates in the accretion disk.

We can therefore determine if the disk is contaminating the system flux by comparing the spectrum of the system to that of a comparison star of similar spectral type to the secondary star. If there are emission features present in the spectrum of the binary, we know that the disk dominates the system flux. Alternatively, if the disk contribution does not dominate, but is significant, some of the absorption features in the spectrum of the system will be weaker than those in the spectrum of the comparison star. We were able to show that we found no evidence for disk contamination in GRO J1655–40.

1.4   An Example of an X–ray Binary

Having discussed the generalities of X–ray binaries, we now turn our attention towards the study of the SXT GRO J1655–40. The main purpose of this thesis was to determine the mass of the black hole in this system. This mass was ascertained by the use of infrared photometry of the ellipsoidal modulation of

GRO J1655–40 to constrain the mass ratio q and inclination i, and by using infrared spectroscopy to constrain the infrared contamination of the accretion disk. We now outline the basics of general photometry and spectroscopy, and discuss the data reduction techniques employed to obtain various information about GRO J1655–40.

Chapter 2

Infrared Astronomy and Data Reduction Techniques

In this chapter, we introduce both photometry and spectroscopy and explore the data reduction techniques we employed to process our observations of a target system.

2.1 Photometry and the Magnitude Scale

Part of this thesis is concerned with determining and modelling the variation in brightness of our observations of our target system. The brightness of this system is measured by a technique known as **photometry**, and the brightness of the object is measured in **magnitudes**, an astronomical scale based on increasing brightness with decreasing magnitude. (This scale dates back to the Greek astronomer Hipparchus in the second century B.C.)

We normally measure the luminosity of the binary over a small range of wavelengths, known as a **photometric band**, rather than measuring the brightness over the entire electromagnetic spectrum. The bands we selected for the observations in this thesis were the $J-$ (1.06–1.44 μm), $K-$ (1.96–2.44 μm) and K_s- (1.99–2.31 μm)[1] bands.

---

[1] The K_s ("K short") filter is a modified K filter that reduces the thermal background for warm ground-based telescopes, as the background at these wavelengths can be significant.

The magnitude of the binary measured by the detector is known as the **instrumental magnitude**. Since this value will vary depending on various factors, such as the photometric conditions and the airmass of the observation, this value can not be immediately compared with earlier observations. We must first make the following corrections, in order to make such comparisons.

2.1.1 Atmospheric Extinction

When a star is observed through the atmosphere, the star is obscured due to the absorption and scattering of the starlight by the atmosphere, a phenomenon known as **atmospheric extinction**.

The amount of extinction for a certain wavelength is known as the **(atmospheric) extinction** for that wavelength, and is given by the product of the **airmass** (χ) and the **extinction coefficient** (k). The airmass is approximately the inverse cosine of the zenith angle of the telescope, and the extinction coefficient is the number of magnitudes of extinction per unit airmass. The value of this coefficient depends on the wavelength observed and the location of the observatory.

If we determine this atmospheric extinction, we can then combine our corrected measurement with that of a photometric standard of known magnitude to obtain the **apparent magnitude** of our target star. This magnitude can be compared to other observations, assuming similar photometric conditions.

2.1.2 Interstellar Extinction

We must also consider the absorption and scattering of starlight due to the dense dust clouds which lie between the Earth and the star. This is known as **interstellar extinction**.

The number of magnitudes of obscuration at a certain wavelength λ is known as the **(interstellar) extinction** A_λ. We can then define two quantities: the **reddening** (E_{B-V}) is the difference $A_B - A_V$, where B is the blue (390–490 nm)

passband and V is the visible (500–600 nm) passband, and the **extinction ratio,** R_V, which is the ratio of the visible extinction to the reddening. This ratio varies, but is usually approximated as

$$R_V = \frac{A_V}{E_{B-V}} \sim 3.1.$$

(2.1)

(See, for example, Cardelli, Clayton, & Mathis 1989.)

To correct for interstellar extinction at a given wavelength, we can use the results of Cardelli, Clayton, & Mathis (1989), who derived the following values for the ratios between the interstellar extinction in the K–band (A_K) and the J–band (A_J), and that in the V–band (A_V):

$$\frac{A_K}{A_V} = 0.114,$$

(2.2)

$$\frac{A_J}{A_V} = 0.282.$$

We can therefore determine an expression for, say, A_K, as follows:

$$
\begin{aligned}
A_K &= 0.114 \times A_V, \\
&= 0.114 \times R_V \times E_{B-V},
\end{aligned}
$$

(2.3)

and then insert the value for R_V (see Equation 2.1) and our measured value for E_{B-V}.

We can then correct the apparent magnitude of the star for the obscuration due to the interstellar medium to obtain the **dereddened magnitude** of the star.

2.1.3   The Intrinsic Brightness of a Star

The final correction that may be made to the magnitude of a star is to account for the distance to the star. For example, although the V–band magnitude of our Sun is -26.8, at a distance of 10 parsecs it would appear as a star of magnitude 4.72. In order to be able to catalog a star according to its intrinsic brightness, we calculate its **absolute magnitude (M)**. This is defined as the magnitude of

the star if observed at a distance of 10 parsecs (pc), and is given by:

$$M \quad = \quad m - 5 \log \frac{d}{10 \, pc}, \quad\quad\quad (2.4)$$

where m is the dereddened magnitude of the star, and d is its distance. For example, the absolute K–band magnitude is given by:

$$M_K \quad = \quad K_0 - 5 \log \frac{d}{10 \, pc}, \quad\quad\quad (2.5)$$

where K_0 is the dereddened K–band magnitude of the star. A similar equation holds for the J–band:

$$M_J \quad = \quad J_0 - 5 \log \frac{d}{10 \, pc}. \quad\quad\quad (2.6)$$

2.2 Spectroscopy

As well as measuring the amount of light from a celestial object using photometry, we can also study the spectrum of that light. This is known as **spectroscopy**. The first application of spectroscopy was the identification of Sodium in the solar spectrum by Fraunhofer in 1814, and the element Helium was discovered spectroscopically in 1868 by studying the Sun. Since these observations, spectroscopy has been employed to determine the chemical makeup of the Sun and other stars.

In this thesis, we need to determine whether there are emission or absorption features present in the spectrum of a binary system, and how strong the spectral features are relative to those in a comparison star. We measure the strength of a spectral feature by calculating the **equivalent width** of the line.

2.2.1 The Equivalent Width of a Spectral Feature

The **equivalent width** of a spectral absorption or emission line is a measure of the strength of the feature, and is defined as the width of a perfectly black line having the same total absorption or emission as the real line. It can be expressed as:

$$|W| = \int \frac{F_c - F_\lambda}{F_c} d\lambda, \qu\quad\quad (2.7)$$

where F_c is the flux due to the continuum, F_λ is the flux at wavelength λ, and the integral is taken from one side of the spectral line to the other. Absorption features are denoted by positive equivalent widths, and emission features by negative widths. Equivalent widths are usually given in Angstroms (Å).

The equivalent width of a spectral line can be thought of as the width of a box of the same area as is under the line, and whose height is the continuum flux value. An example of such a representation is given in Figure 2.1.
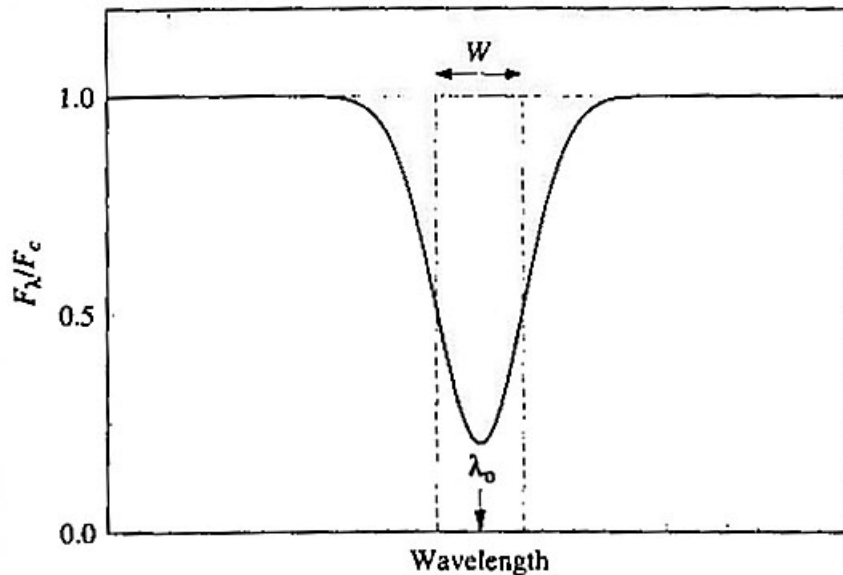
Figure 2.1: Example of a spectral absorption line at $\lambda = \lambda_0$, indicating the equivalent width W of the feature (Carroll & Ostlie 1996).

2.2.2 The Radial Velocity of the Secondary Star

We used spectroscopy in order to verify that the disk in our target system was not contaminating the light curve of the binary. We also measured the **radial velocity** of the secondary star, so as to confirm that our spectra were consistent with past observations. This was especially necessary as these were the first high signal-to-noise K–band spectra of a black hole X–ray transient system.

The radial velocity of the secondary star in a binary system may be calculated from:

$$v_r = \gamma + K_2 \sin{(2\pi\phi)}, \tag{2.8}$$

where γ is the systematic velocity of the binary system, and ϕ is the orbital phase of the binary.

The radial velocity can be measured from the Doppler shift of the observed wavelengths of the spectral features in the spectrum of the star, which is a result of the motion of the star relative to the observer along their line of sight. This shift is given by:

$$\begin{aligned} \Delta\lambda &= \lambda_{\text{obs}} - \lambda, \tag{2.9} \\ &= \frac{v_r \lambda}{c}, \tag{2.10} \end{aligned}$$

where λ and λ_{obs} are the rest and observed wavelengths, respectively, of the spectral feature. Therefore, if we know $\Delta\lambda$, we can also calculate the radial velocity from:

$$v_r = \frac{\Delta\lambda}{\lambda} c. \tag{2.11}$$

We compared the predicted radial velocity of our target star (calculated using the published spectroscopic ephemeris) with that determined from the $\Delta\lambda$ measured from the spectrum of the star, to ensure that our result agreed with prior observations of GRO J1655–40.

2.3   Advantages of IR Observations of GRO J1655–40

This thesis is concerned with the infrared observations of the X–ray binary GRO J1655–40. Although X–ray binaries emit energy primarily as X–rays, our observations of GRO J1655–40 were made at infrared wavelengths, (the J–, K– and K_s–bands). This section explains the advantages for doing so, as well as the drawbacks of infrared observations.

Dominance of Secondary

A luminous accretion disk in a binary system will be bluer than the secondary star, and should contribute less in the infrared than in the optical. Hence this intrinsic emission from the secondary star should dominate in the infrared, and this will allow a better estimate of the brightness of the secondary to be made. This increases the likelihood of tightly constraining the mass ratio, inclination and black hole mass through infrared observations.

Disk Contamination and Infrared Spectroscopy

If we ignore the accretion disk contribution for a given binary system, we cannot be certain that we are not underestimating the orbital inclination for that system, or that our derived stellar masses are valid estimates. Although the quiescent infrared disk contribution is often assumed be negligible (see, for example, Shahbaz, Naylor, & Charles 1994), it is possible that the disk can in fact be a strong source of infrared radiation. Infrared spectroscopy can be used to constrain the level of accretion disk contamination in the infrared during quiescence.

Interstellar Extinction

In general, the K–band interstellar extinction, A_K, is nine times smaller than visual band extinction, A_V ($A_K \sim 0.114\, A_V$: Cardelli, Clayton, & Mathis 1989). Therefore, the interstellar medium absorbs less infrared radiation than optical. Hence any attempt to locate a faint distant object may be more successful if the observations are made in the infrared.

More specifically, we will later show that our target system GRO J1655–40 has a high visual extinction of $A_V = 4.0 \pm 0.3\,\mathrm{mag}$, but a low infrared extinction $A_K = 0.42 \pm 0.04\,\mathrm{mag}$ (see § 4.1.4 on page 55). This system is therefore less obscured in the infrared, which improves the quality of images taken at these wavelengths.

Improved Spatial Resolution

More generally, the resolution of an observation specifies the minimum angular separation required between two stars for the pair to be distinguishable. At wavelengths less than or equal to infrared wavelengths (1.0–$2.4\,\mu$m), and for 1-m or larger telescopes, this resolution is determined mainly by the effect of turbulence in the atmosphere (see, e.g., Schroeder 1987 for details). In this regime, there is an improvement in resolution with increasing wavelength, as the longer wavelengths are less refracted by the atmosphere than the shorter wavelengths. Therefore, the infrared offers better quality images than the optical (400–$700\,$nm).

Disadvantages

The main disadvantage of infrared photometry is that the background is much higher relative to that at, for example, optical wavelengths. Before any meaningful analysis can be made, the thermal background from the atmosphere and even the instruments and the telescope used to make the observations must be accounted for.

Also, in order to obtain useful infrared spectra, the atmospheric absorption or **telluric** features caused by the presence of oxygen and water vapour in the Earth's atmosphere must be accurately subtracted. The OH lines in the atmosphere would otherwise dominate the spectra. This increases the difficulty of data reduction in comparison to optical spectroscopy.

Once we make our infrared observations of a target star, we have to perform either photometric or spectroscopic data reduction to obtain information about our system of interest.

2.4   Reduction of Infrared Photometric Data

We can employ photometry to determine the brightness of a binary star from infrared observations of that star. The raw images of the star are first processed to improve their quality. This is known as **Image Reduction**. Then we obtain

the magnitude of the target star relative to several comparison stars in each processed image. The images are calibrated to obtain the apparent magnitudes of the chosen stars in the sky. Finally, the absolute magnitude of the target star is calculated, taking its distance and interstellar extinction into account.

2.4.1 `IRAF` and `DS9`

Much of the image reduction and data analysis performed can be done using the **Image Reduction and Analysis Facility (IRAF)** package (v 2.11.3), a product of the U.S. National Optical Astronomy Observatories (NOAO). The `IRAF` tasks and packages that we run are denoted in this section by `typewriter` font. The task parameters and their values are written using the *italic* font.

Occasionally throughout the reduction and analysis, it is necessary to view and interact with the images. Our image viewer is **SAOIMAGE DS9** (v 2.1b4), written by the Smithsonian Astrophysical Observatory Research and Development Group.

2.4.2 Image Reduction

Our observations involve centering the telescope on the target and then obtaining a group of images – normally nine images are obtained per group. The images form a grid, with each image offset by approximately 10% of the field of view from a common point in the sky.

For each grid of $K-$ or $J-$band images, the following procedure is performed to produce a high-quality image from which the magnitude of the star can be determined. (More comprehensive details of elements of the photometric image reduction procedure may be found in § A.2 on page 82.)

2.4.3 Background Subtraction

As mentioned on page 28, the use of infrared observations suffers from the disadvantage that the background level is higher than for observations obtained at, for

example, optical wavelengths. Unprocessed source images therefore reveal little, as most of the stars are obscured by this background. Nevertheless, it is possible to estimate the background and subtract it from the raw images, resulting in superior data.

An image is created from the grid of images using the `imcombine` command. The parameter *combine* is set to *median*, that is, the value of each pixel is taken to be the median value of that pixel over the images in the grid. As long as the pixel detected flux from a star in less than half of the images (i.e., the observed field was not crowded), this median value should be an approximation of the background level at that pixel. This assumes that the background did not vary as the telescope pointing changed, and that it was constant over the time of the observation. Since the cloud cover, wind speed and atmospheric temperature are often more or less constant for this period of time (about 30 mins), the approximation is normally accurate. The median pixel file, called the **background image**, is therefore used to subtract the background from the original images using `imarith`. A new background file is created for each grid of images.

2.4.4   Flatfield

Having subtracted the background image, we then take into account the intrinsic pixel to pixel variations for the observed wavelengths. To do this, a **flatfield image**, which represents this variability, is created using one of the following methods.

The first method is to make a **dome flat**. During the observation run, an image of an illuminated spot inside the closed observatory dome is obtained, as well as an exposure of the spot without illumination but with the same integration time. This procedure is repeated several times throughout the period of observations. The two sets of illuminated and non-illuminated images are then `imcombine`d (with *combine=average*) separately so as to obtain an averaged illuminated and non-illuminated image, respectively. Using `imarith`, the non-illuminated image is subtracted from the illuminated image. The resultant

subtracted image is divided by its median pixel value (obtained from `imstat`) to obtain the flatfield image. The background subtracted images are then divided by the flatfield.

An alternative method is **median combination**, which can be used if no dome flats are obtained during the observation run. First, all the images obtained during the run are `imcombine`d using the median value for each pixel. Once more, it is assumed that in a sparse field, this median value represents the background. Second, the median pixel value of the median image is obtained from `imstat`, and the image is divided by this value (again using `imarith`). Third, the resultant image is taken as an approximation of the relative response of each pixel, and the subtracted images are divided by this flatfield.

2.4.5   Bad Pixels

Some of the pixels in a detector may not respond properly to radiation of any wavelength, and record an excessively high or low value for the incident flux. These pixels, known as **bad pixels**, should be disregarded when viewing the background subtracted, flatfielded images. This is done automatically by creating a **bad pixel map**.

Firstly, the raw images are median combined and the resultant image divided by its overall median pixel value, in a similar manner to the median combined flatfield method discussed above. Secondly, the value of each pixel in the divided image is written to a text file using the `listpixel` command. Since the average value of a pixel in the divided image should have been approximately 1, the pixels that registered a value of below 0.75 or above 1.25 are chosen as the bad pixels for the detector. These pixels are used by the `badpiximage` command to create a bad pixel map.

2.4.6   Combining the Grid

We can now combine all the processed images to produce high quality images of our target.

If all the images taken are of the same field of view, a common point in the images can be selected, which is in the central region of each image. The background subtracted and flatfielded images are then shifted using the `imshift` command, so that this common point is at the same coordinates in each image. The corresponding bad pixel map previously created is also shifted for each image, so as to account for the relocation of the bad pixels in that image.

Using `imcombine`, each grid of frames are average combined. The combined images are then visually examined, and those of unacceptable quality are discarded.

2.4.7 Relative Photometry

Once processed images have been acquired, it is possible to determine the brightness of the stars in the field of view. For the purposes of studying the variability of systems like GRO J1655–40, we need only the brightness of the system relative to a star of constant brightness. Nevertheless, in order to compare our observations with previous ones, we also require a calibrated measure of the brightness of the system.

Relative or **differential photometry** is the calculation of the magnitude of one star relative to another. This technique is useful because, although the observed magnitudes of two constant, neighbouring stars may appear to vary in time (due to changing atmospheric conditions), the magnitude of one relative to the other should not. Therefore, if we determine the magnitude of our target star relative to a constant star in the field of view, we can attribute any variation in this value to the changing intrinsic magnitude of our star.

Relative photometry can be carried out using the `IRAF` adaptation of the `DAOPHOT` package for crowded field stellar photometry (Stetson 1987). (See § A.2.4 on page 85 for details of this procedure.) Firstly, we select a constant star (which we denote as our **comparison star**) of comparable brightness to our target star, and several bright constant stars in the field of view (our **reference stars**). These stars, together with our target star, are denoted as our stars of interest.

Secondly, `DAOPHOT` is run to remove near neighbours of the selected stars. Several isolated faint stars in the field of view are chosen as model stars, and are used by `DAOPHOT` to create a **point spread function (PSF)** model. This PSF model is then fitted to all our stars of interest and the instrumental magnitudes are obtained from `allstar`. The magnitudes of the reference stars are averaged, and this value subtracted from the magnitude of the target star and the comparison star. The Julian Date of each observation is determined from the Universal Date and Time. The two relative magnitudes are plotted against the Julian Dates of the observations to obtain the light curves of the target and comparison star. The light curve of the comparison star generated in this way can be used as a measure of the error in our target star light curve. If we know the orbital ephemeris of the target star, we can then fold the light curve of the target star to search for systematic variations as a function of orbital phases.

Finally, in order to estimate the average magnitude of the possibly variable star, we obtain the **phase averaged relative magnitude**: we average the values for the magnitude of our target star relative to one particular reference star.

2.4.8   Aperture Photometry and Photometric Calibration

Although we now have the magnitude of our star relative to a constant star, we don't know the actual magnitude of the star itself. This we estimate by first manually determining the instrumental magnitude of the star using **aperture photometry**, and then calculating the apparent magnitude of the system.

First, we obtain the counts per second (f_{10}) detected by our telescope from a star of known magnitude, say magnitude 10. We then (i) determine the number of counts per second measured from this comparison star, (ii) correcte this for atmospheric extinction, and (iii) comparee this to f_{10}, to obtain the apparent magnitude of the comparison star.

This process is performed for both the $J-$ and K_s-band observations. This magnitude is then used to calibrate the (phase averaged) magnitude of our target star, allowing us to finally calculate the phase averaged K_s- and $J-$band apparent

magnitudes of our target star.

2.4.9 Dereddened and Absolute Magnitudes

We can now calculate the **dereddened magnitude** of the star by determining the necessary corrections to account for interstellar extinction (see § 2.1.2 on page 22).

If we know the value of E_{B-V}, we can calculate the K–band extinction from Equation 2.3 on page 23:

$$A_K \quad = \quad 0.114 \times R_V \times E_{B-V},$$

and similarly for the J–band extinction. Then, the dereddened magnitude (K_0) of our target star in the K–band can be found via:

$$K_0 \quad = \quad \text{apparent } K_s \text{ magnitude} - A_K, \tag{2.12}$$

and similarly for the J–band.

The last step in the photometric data reduction is to calculate the absolute magnitude of the target star. Assuming we know the distance to the star, the J and K absolute magnitudes of the star can then be calculated using Equations 2.5 and 2.6.

2.5 Reduction of Infrared Spectroscopic Data

Just as we need to correct our photometric data for the background and detector pixel variations, we need to process our spectra to (i) account for the background, (ii) apply a dispersion correction, and (iii) remove telluric features. The corrected spectra can then be averaged to obtain our final target spectrum. (Further details on the steps in the procedure for the reduction of the spectroscopic data can be found in § A.3 on page 86.)

2.5.1 Background Subtraction

The first step in producing processed spectra is to subtract the background from each of the observations. We can do this by selecting two images of our star, and subtracting one from the other and vice versa. In this way, we obtain two subtracted images of the star. Since the object appears at different places on the slit in the two original images, there is no overlap of the object spectrum between the images. This subtraction is done for the spectra of each star.

2.5.2 Spectra Extraction

The background subtracted images are then processed using `apall` to obtain 1-D spectra for each star. An Argon arc lamp spectrum is also extracted for each star, using the trace for the star to trace the corresponding arc.

2.5.3 Wavelength Calibration

The extracted spectra are plotted to display the flux from the star detected by each pixel of the detector. However, in order to compare the spectra with previous observations, we need to determine the flux as a function of wavelength. This calibration of the spectra is done by using our extracted arc spectra as a reference. The known wavelength of each Ar feature is compared to the pixel value at which the feature is observed in the arc spectra. The `identify` and `reidentify` tasks are then run to calculate a dispersion correction to obtain a corresponding wavelength for each pixel. This dispersion correction is then applied by `dispcor` to the extracted spectra.

2.5.4 Normalisation

To study the absorption and emission features in the spectra, it is useful to normalise the spectra to the continuum flux. We normalise our wavelength-callibrated spectra by using the task `continuum` to fit the continuum of each spectrum to a spline of order 2.

2.5.5 Removing Telluric Features

Next, the telluric features present in raw spectra must be removed. This is especially important in the infrared, where atmospheric features can dominate the spectra.

The telluric features can be accounted for by dividing the target star spectra by the spectrum of a nearby star. This method assumes that both stars are affected in the same way by the telluric features, and hence dividing one by the other should, in theory, cancel this effect. This method has a systematic error, in that the absorption features present in the nearby star will be seen as emission features in the divided spectra. This effect can be minimised by choosing a star with few prominent spectral features.

An A0-type star may be chosen as the comparison star because of the large effective temperature of stars of this classification, which results in a spectrum with only one prominent feature in the K–band. This is the neutral hydrogen absorption line H I (4–7) at $\lambda = 21\,655\,\text{Å}$, known as the Brackett-$\gamma$ (Br-γ) absorption feature. We then assume that the other features in our spectra of our comparison star are telluric. This feature is masked and the resulting A0 spectrum is divided into the target spectrum to remove the telluric features.

2.5.6 Combining the Spectra

The two target star spectra, corrected for telluric features using the comparison star, are combined using `scombine` (*combine* set to *average*). The resultant spectrum is smoothed using `splot`, with a bin size of 3, to obtain the final spectrum.

2.6 Our System of Interest

We now consider GRO J1655–40 in detail and present the reasons for studying this transient. We will then apply the data reduction techniques we have outlined to this system, and attempt to obtain an estimate for the mass of the primary star within this binary system.

Chapter 3

GRO J1655–40

In this chapter, we first detail the system properties of GRO J1655–40, with emphasis on the accretion disk surrounding the primary star. We list the observations we made of this SXT, and also elucidate the general reasons for studying this system.

Our specific reason for studying GRO J1655–40 is to obtain an estimate of the mass of the black hole which this system is thought to harbour. If we assume that the accretion disk contributes little to the total flux from the system, we can then constrain the mass ratio q (and hence the primary mass M_X) and the inclination i from the ellipsoidal modulation of the binary and the radial velocity curve.

We will therefore later explain how we applied infrared photometric techniques to obtain the light curve of GRO J1655–40 during the period of our observations, and show how we determined the mass of the black hole from the light curve, before discussing whether our assumption of negligible disk contamination is valid.

3.1 Introduction to GRO J1655–40

In July 1994, GRO J1655–40[1] was observed for the first time by the Burst and Transient Source Experiment (BATSE) onboard the Compton Gamma Ray Observatory (CGRO) (Zhang et al. 1994). Four outbursts in total were observed in the first five months after its discovery (Harmon et al. 1995). The optical counterpart of this system was identified in 1995 by Bailyn et al. (1995a), the mass function derived by several observers (e.g., Orosz & Bailyn 1997) for the primary star in GRO J1655–40 indicated that this system might contain a black hole.

3.1.1 General Properties and Special Characteristics

System Properties

GRO J1655–40 lies approximately 3.2 kiloparsecs (kpc) away (Hjellming & Rupen 1995). Hynes et al. (1998) derived a reddening E_{B-V} of $1.2 \pm 0.1\,\mathrm{mag}$ for GRO J1655–40, from which they calculate a hydrogen column density of $N_H \sim 5 \times 10^{21}\,\mathrm{cm}^{-2}$. From these values, the quiescent bolometric luminosity of GRO J1655–40 can be determined to be approximately $41\,\mathrm{L}_\odot$ (see, e.g., van der Hooft et al. 1998). The quiescent V–band magnitude of GRO J1655–40 is approximately 17.1 mag (Greene, Bailyn, & Orosz 2001), and the system becomes as bright as 16.2 mag in the V–band during outburst (Bailyn et al. 1995b).

The times of the inferior conjunction of the primary are described by the following photometric ephemeris (van der Hooft et al. 1998), given in MJD[2] :

$$
\begin{aligned}
T_{\min}\,(\mathrm{MJD}) &= T_0 + P \times N, \\
&= 49838.4198(52) + 2.62168(14) \times N, \quad\quad (3.1)
\end{aligned}
$$

where T_0 is the time of mid–eclipse, P is the orbital period and N denotes the number of orbital cycles.

The most recent values for the mass ratio and inclination of GRO J1655–40

---

[1] The SIMBAD identifier of GRO J1655–40 is V* V1033 Sco. It is also referred to as **Nova Scorpii 1994 (Nova Sco 1994)**.

[2] The **Modified Julian Date (MJD)** is defined to be the Julian Date (JD) minus 2400000.5.

are those predicted by Beer & Podsiadlowski (2002). They derived values of $q = 3.9 \pm 0.6$ and $i = 68^\circ\!\!.65 \pm 1^\circ\!\!.5$. Using the mass function of Shahbaz et al. (1999), $f(M_X) = 2.73 \pm 0.09\,M_\odot$, they determined that GRO J1655–40 consists of a $5.4 \pm 0.3\,M_\odot$ black hole primary and a $1.45 \pm 0.35\,M_\odot$ secondary. The secondary is a giant (or subgiant) of spectra type F5–G0, and orbits at a distance of approximately $16.6\,R_\odot$ from the primary.

Anomalies

GRO J1655–40 displays several atypical characteristics:

- GRO J1655–40 is optically the brightest in quiescence of all SXTs. The secondary dominates in quiescence to an unusually large extent, due its relatively luminous F/G star nature. The light curves of GRO J1655–40 are therefore unusually smooth and symmetrical when compared to those of other black hole binaries, and so the measurements of the mass ratio and inclination of this system should therefore be atypically precise.

- GRO J1655–40 is one of three known Galactic X–ray sources with apparently superluminal jets – another being GRS 1915+105 – (see Tavani et al. 1996 and references therein), and is the only such source to be identified optically. GRO J1655–40 is also less obscured by dust than GRS 1915+105, and is hence more easily studied. The jets were discovered by Tingay et al. (1995) and were shown to have actual speeds of $0.92 \pm 0.02\,c$ by Hjellming & Rupen (1995).

- Most other SXTs have shorter periods and smaller accretion disks (Hynes et al. 1998).

- Kolb et al. (1997) suggested that GRO J1655–40 is in a different evolutionary state to other SXTs. Although the secondary stars in SXTs are evolved, the secondary in GRO J1655–40 is an extreme case, and has almost become a giant.

- GRO J1655–40 has an unusually high accretion rate ($\dot{M}_2$), which is close to its critical value ($\dot{M}_{\mathrm{crit}}$): these rates were calculated by Orosz & Bailyn

(1997) to be $3.4 \times 10^{-9} \, \mathrm{M_\odot \, yr^{-1}}$ and $1.1 \times 10^{-8} \, \mathrm{M_\odot \, yr^{-1}}$, respectively. This implies that GRO J1655–40 is likely to have frequent X–ray outbursts.

- GRO J1655–40 is the only SXT to show evidence of eclipses, as observed by Bailyn et al. (1995a) at optical wavelengths. These eclipses are of the accretion disk and suggest that i is large. However, no eclipses are observed in the X–ray, which implies that the compact object is not eclipsed by the secondary star, and negates the possibility that $i \sim 90°$ (Orosz & Bailyn 1997). Nevertheless, Zhang et al. (1997) noted that the high inclination angle of GRO J1655–40 is the largest amongst all well-known Galactic black hole binaries.

- The systematic velocity of GRO J1655–40, $\gamma = -142.4 \pm 1.6 \, \mathrm{km \, s^{-1}}$ (Orosz & Bailyn 1997), is atypically high for a LMXB containing a black hole. This value is more suggestive of a neutron star binary. Brandt et al. (1995) suggested that the progenitor of the primary star in GRO J1655–40 did not collapse directly into a black hole. Rather, it was formed when a neutron star evolved into a black hole due to the accretion of additional mass. This evolutionary process would account for the abnormal γ–velocity. Mirabel et al. (2002) confirmed that both the systematic velocity and the high galactocentric eccentricity ($e = 0.34 \pm 0.05$) of this system could be explained by a natal explosion.

3.1.2 Reasons to Study GRO J1655–40

If we can assume a negligible disk contribution, the unique ellipsoidal variations and eclipses of GRO J1655–40 should allow us to constrain the mass ratio and inclination considerably. This will lead to a unprecedented precision in the measurement of the mass ratio and orbital inclination – see, for example, Orosz & Bailyn (1997). The high precision in q and i in return should enable a similarly precise value for the mass of the primary to be determined, strengthening the evidence for the black hole nature of this star.

GRO J1655–40 is also important due to its superluminal jet nature. The

study of Galactic superluminal X–ray sources is important as it may lead to a better understanding of **Active Galactic Nuclei (AGN)**. These show similar jet geometry to these Galactic sources, possibly due to comparable conditions of accretion. AGN are thought to be powered by massive ($\lesssim 10^{10} \, \mathrm{M_\odot}$) black holes and may be the high-luminosity counterparts to sources such as GRO J1655–40.

Finally, further study of the eclipses in GRO J1655–40 may lead to information on the structure of the disk in this system. GRO J1655–40 therefore could be the best X–ray binary with which to test various models of X–ray production and jet formation in the search for a better understanding of AGN.

3.1.3   The Accretion Disk Contribution in GRO J1655–40

When modelling SXTs, it is often assumed that the accretion disk contributes little light to the overall system flux during quiescence (see page 27). Indeed, the spectral type of the secondary star in GRO J1655–40 is earlier than that in most other SXTs, implying that any small contamination due to an accretion disk would be less significant than in the other systems (Beer & Podsiadlowski 2002). However, it is important to verify the above assumption for GRO J1655–40, if the derived system parameters are to be believed.

Bailyn et al. (1998) note that the disk in GRO J1655–40 is redder than the secondary during quiescence. The unusually long period of this system implies that a large disk can form, the outer parts of which will be cooler than in other systems. These characteristics imply that there may be more flux at the longer wavelengths, such as the infrared. This questions the validity of the assumption that the quiescent disk contribution is negligible, even though there is no evidence of such a contribution from photometric measurements (see, for example, Greene, Bailyn, & Orosz 2001). Therefore, the disk contribution must be shown to be inconsequential using other methods such as spectral analysis, if we are to accurately determine the orbital inclination and mass ratio of GRO J1655–40.

3.2 Observations of GRO J1655–40

3.2.1 The Observatories and the Instruments

The Cerro Tololo Infrared Imager at CTIO

The 1995 and 1998 photometric observations of GRO J1655–40 were made using the 1.5m Ritchey-Chretien telescope at the **Cerro Tololo Interamerican Observatory (CTIO)** located in Chile. The **Cerro Tololo Infrared Imager (CIRIM)**[3], a mercury-cadmium-telluride (HgCdTe) 256×256 NICMOS 3 array with a variable pixel scale, was the detector used.

The J– and K_s–band extinction coefficients, k_J and k_{K_s} (see page 22), at the observatory were previously measured to be approximately 0.11 mag/airmass and 0.064 mag/airmass, respectively (Curran 2001).

The Near Infrared Spectrometer at KECK

Photometric and spectroscopic data for GRO J1655–40 were taken in 2000 at the 10m Keck II telescope at the **W.M. Keck Observatory (KECK)** in Mauna Kea, Hawaii.

The instrument selected for the spectroscopy was the **Near Infrared Spectrometer (NIRSPEC)**[4], a vacuum-cryogenic, high-resolution spectrograph for the Keck II telescope.

As part of NIRSPEC, the infrared **Slit-viewing Camera (S-CAM)** operates over the wavelength region 0.95–2.5 microns. This HgCdTe array has 256×256 pixels and a field of view of $46'' \times 46''$ (a pixel scale of $0.183''$/pixel). This detector was used to obtain several images of GRO J1655–40 for use in calibration.

The extinction coefficient in the K–band, k_K, at the KECK observatory is known to be ~ 0.088 mag/airmass (Curran 2001).

---

[3] http://www.ctio.noao.edu/instruments/ir_instruments/cirim/cirim.html

[4] http://www2.keck.hawaii.edu:3636/realpublic/inst/nirspec/nirspec.html

3.2.2 Details of the Observations

See Table 3.1 for an overview of the observations.

1995 Photometry

GRO J1655–40 was observed using the CIRIM J– and K_s–filters on 1995 June 8–13 UT. The f/13.5 focus was selected, giving a pixel scale of 0.65 arcseconds per pixel (with a corresponding field of view of $166'' \times 166''$) for our observations. The photometric conditions varied over the run, with seeing typically $\sim 1.5''$.

For each observation, the telescope was centered on the target and a grid of images was obtained. For the 1995 and 1998 CTIO data (see later), normally nine images were obtained per grid.

Table 3.1: Journal of Photometric Observations of GRO J1655–40

Year	Start[a] (UT)	End[a] (UT)	Start (MJD)	End (MJD)
1995	1995 06 08 02:13:27	1995 06 13 02:37:36	49876.59267	49881.60844
1998	1998 05 30 01:46:09	1998 06 04 09:26:20	50963.57372	50968.89329
2000	2000 07 24 06:23:52	2000 07 24 06:53:07	51749.76657	51749.78689
Year	Integration Time (s)	Coadds	Images (J)	Images (K or K_s)
1995	15	5	9	225
	3	5	–	9
1998	30	4	18	162
	15	4	63	–
2000	10	1	–	19

[a]YYYY MM DD HH:MM:SS

Table 3.1 summarizes the observations made of GRO J1655–40 during 1995 June as well as the periods in 1998 and 2000. The observations made in 1995 were obtained while the system was in outburst (Harmon 1996).

1998 Photometry

Photometry of GRO J1655–40 was obtained in the $J-$ and K_s–bands using the CIRIM detector during 6 nights between 1998 May 30 and 1998 June 4 UT. The variable pixel scale was again set at 0.65 arcseconds per pixel. These observations were made while the system was in a quiescent state.

The airmass for each observation was in the range 1.2–2.2 for the K_s–band, and 1.1–2.0 for the J–band. Seeing during the run was $\sim 1.4''$.

2000 Photometry

On 2000 July 24 UT, images of GRO J1655–40 were obtained in the K–band using the NIRSPEC camera. The fixed pixel scale of $0.183''$/pixel gave a field of view of $46'' \times 46''$. Of the 19 images, 6 were selected to form a grid.

The range of airmasses was 1.98–2.02, and the conditions were excellent, with a seeing of approximately $0.7''$.

2000 Spectroscopy

GRO J1655–40 was observed spectroscopically in the K–band using the NIR-SPEC spectrograph on 2000 July 24 UT, using a slit of width $0.57''$ and orientated approximately east-west. The resolution of the spectra was $11.2\,\text{Å}$. The airmass for the observations ranged from 1.057 to 2.087.

An A0 type star (HD 326320) was also observed using similar spectroscopic settings, and several Ne and Ar arc lamp spectra were obtained in the K–band.

See Table 3.2 for a more detailed description of the spectroscopic observations made.

3.3   Obtaining the Light Curve of GRO J1655–40

Next we discuss how we applied the data reduction techniques explored in § 2 to obtain a light curve for GRO J1655–40 showing the intrinsic variability of the

Table 3.2: Journal of Spectroscopic Observations

Start (UT)	End (UT)	Start (MJD)	End (MJD)
2000 07 24 06:21:51	2000 07 24 07:18:35	51749.76517	51749.80457
Target	Integration Time (s)	Coadds	Images (K)
GRO J1655–40	300	1	2
HD 326320	20	1	2
Neon Arc Lamp	5	1	2
Argon Arc Lamp	5	1	2

system.

Chapter 4

The Light Curve of
GRO J1655–40

The initial step in calculating the mass of the black hole in GRO J1655–40 is to measure the ellipsoidal variability of the system. Here we explain how we obtained the light curve of GRO J1655–40 from our observations.

4.1   Photometry of GRO J1655–40

For the CTIO and KECK J– and K–band observations, we performed the following procedure to produce light curves for each period of observation.

4.1.1   The Initial Data Reduction

First, the images were background subtracted, as discussed in § 2.4.3, to remove the high background typical of infrared images.

Second, a **dome flat** was produced for the 1998 CTIO data, and the alternative method of **median combination** was employed to create a flatfield for the 1995 CTIO images (see § 2.4.4). However, dome flats were not obtained for the KECK images of GRO J1655–40: since the total number of raw images obtained using the KECK telescope was too small for an accurate flatfield to be produced (using the median combination technique), the KECK images were not divided

by any flatfield.

Third, a bad pixel map was produced in the manner described in § 2.4.5 for the 1998 and 1995 data sets. Due to the small number of KECK images, no bad pixel map was created for the KECK data. However, a visual inspection of the KECK images determined that no bad pixels were present near the target stars.
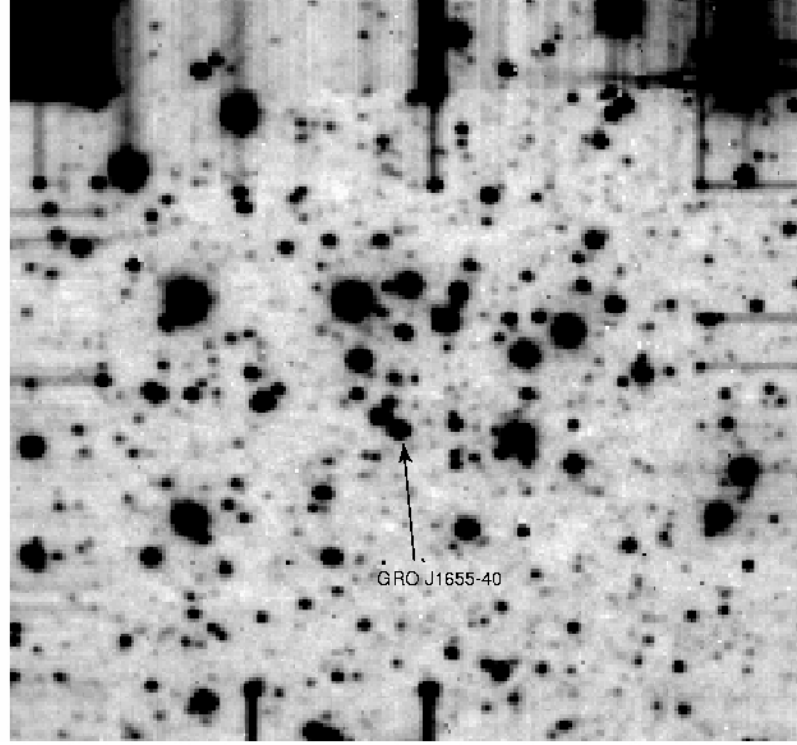
Figure 4.1: Example of an average combined grid of frames, with our system of interest (GRO J1655–40) indicated. This 15 second exposure, which has a field of view of $\sim 166'' \times 166''$, was obtained using the CTIO CIRIM detector during June 1995.

Finally, each grid of images were combined to produce processed images of our target system (see § 2.4.6 on page 31 for details). Figure 4.1 is an example of a combined grid from the 1995 K_s–band data set.
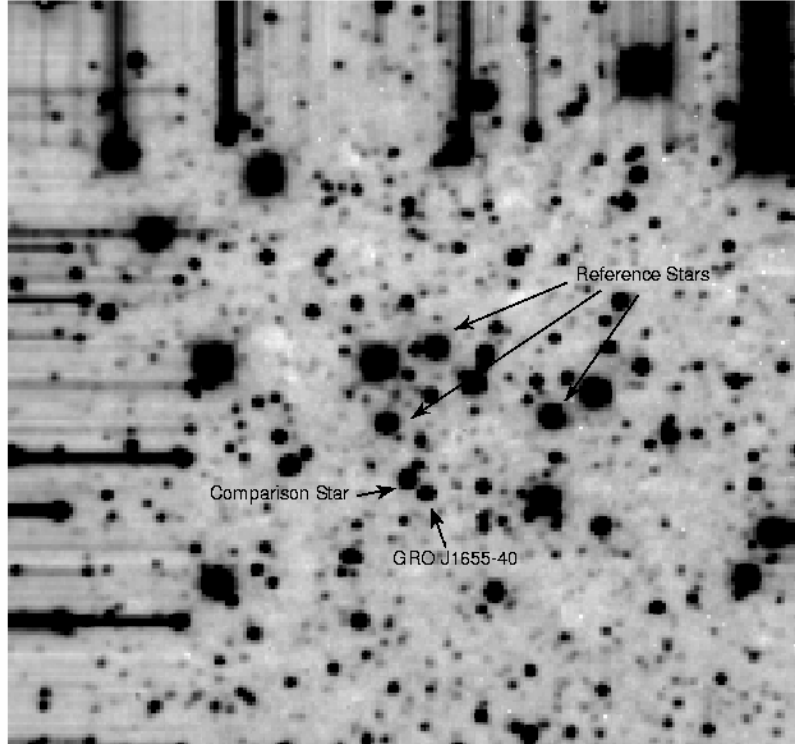
Figure 4.2: Field of view for the 1998 K_s data, indicating the target, comparison and reference stars. This $\sim 166'' \times 166''$ image was obtained with a 30 second exposure using the CTIO CIRIM detector during June 1998.

4.1.2 Calculating the Relative Magnitudes

Once the raw images were processed, we proceeded to run `DAOPHOT` to measure the magnitudes of GRO J1655–40 and a comparison star relative to several reference stars in the same field of view. The procedure outlined in § 2.4.7 was used for each period of observation and each filter. The stars chosen are given in Figure 4.2.

We then plotted the two relative magnitudes against the Julian Dates of the observations to obtain the light curves of the target and comparison star (see Figure 4.3). Since the relative magnitude of the comparison star was constant over this period of observation, we assumed that the variability in the relative magnitude of GRO J1655–40 was due to the changing magnitude of the system itself.
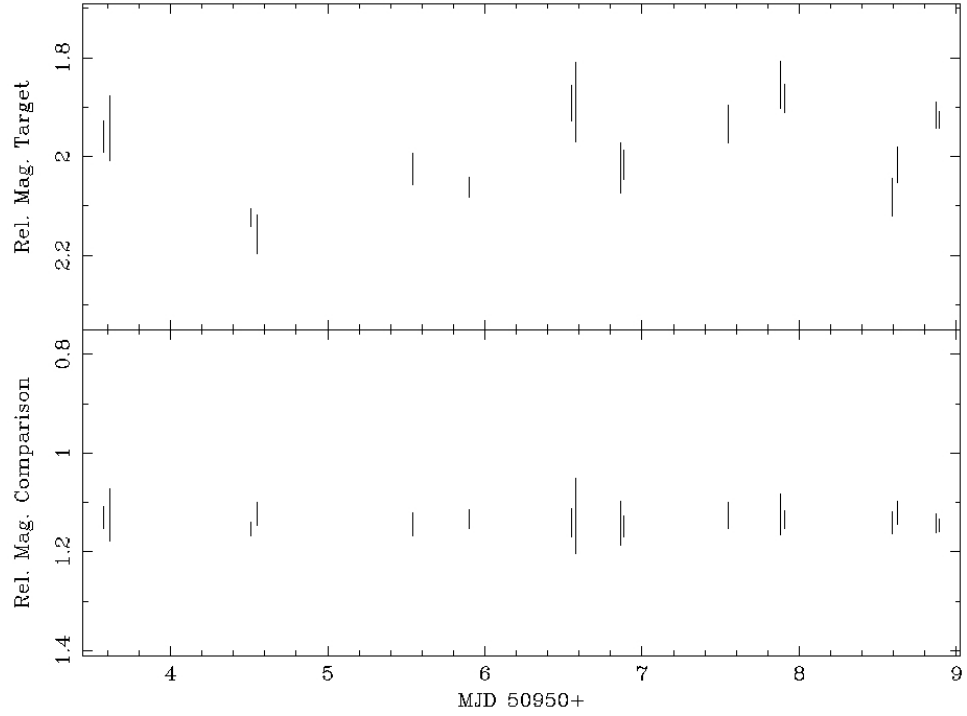
Figure 4.3: Plot of relative magnitudes of target star GRO J1655–40 and comparison star for the 1998 K_s observations.

Finally, using the orbital ephemeris determined by Van der Hooft et al. (1998) (see § 3.1 on page 38), we folded[1] the light curve of GRO J1655–40 on the orbital period. We then introduced an offset to the 1998 K_s data to move one of the points to phase 0.5, and so align the minima and maxima with the appropriate phases. This offset was within the error of 3% incurred by extrapolating the ephemeris to the time of observation.

Figure 4.4 and Figure 4.5 show the folded K_s light curves for each year. As can be seen from Figure 4.5, an ellipsoidal variability was apparent from the 1998 K_s light curve.

---

[1]When folding the data, the Heliocentric Julian Date (HJD) of the observation was taken to be equal to the Julian Date (JD) of observation. Although this introduced an error of 8 minutes, this is small compared to the error in the orbital period ($2^d.62168 \pm 0^d.00014$: van der Hooft et al. 1998).
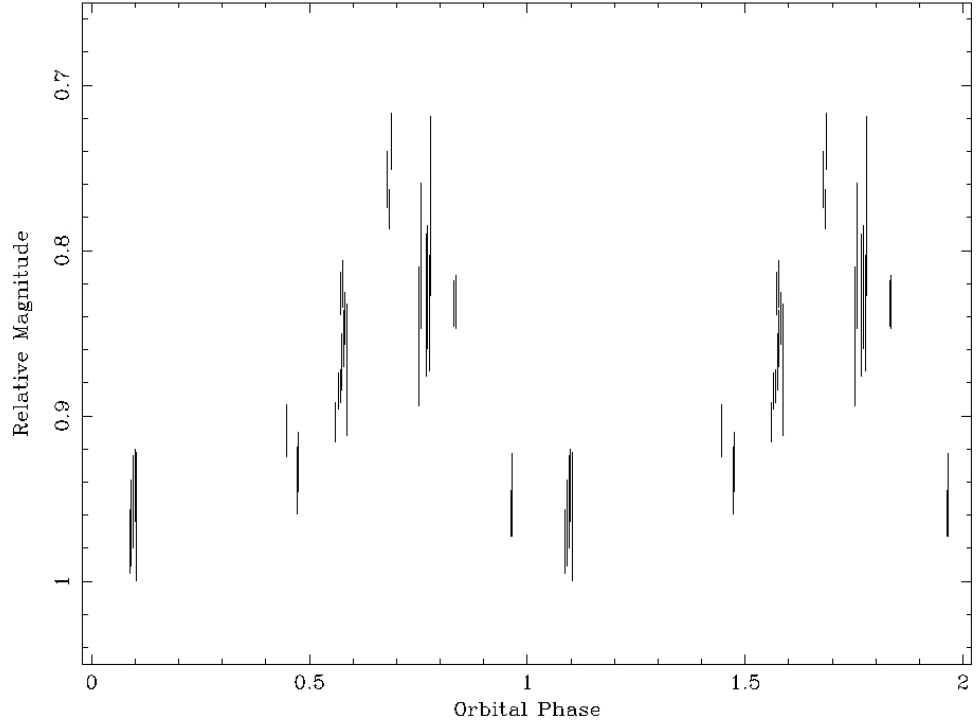
Figure 4.4: The light curve of GRO J1655–40 during June 1995. The fold is repeated for clarity.

Using the folded light curves, we then calculated the phase averaged relative magnitudes of GRO J1655–40 (see § 2.4.7). Since the 1995 J–band data consisted of only one combined image, it was not possible to get the phase average relative magnitude of GRO J1655–40. The relative magnitude of GRO J1655–40 in the single image was taken as the average. Table 4.1 lists the averaged magnitudes calculated.

Table 4.1: GRO J1655–40 Phase Averaged Relative Magnitudes

Year	J Relative Magnitude (mag)	K_s Relative Magnitude (mag)
1995	0.01 ± 0.05	0.68 ± 0.05
1998	1.00 ± 0.05	1.71 ± 0.05
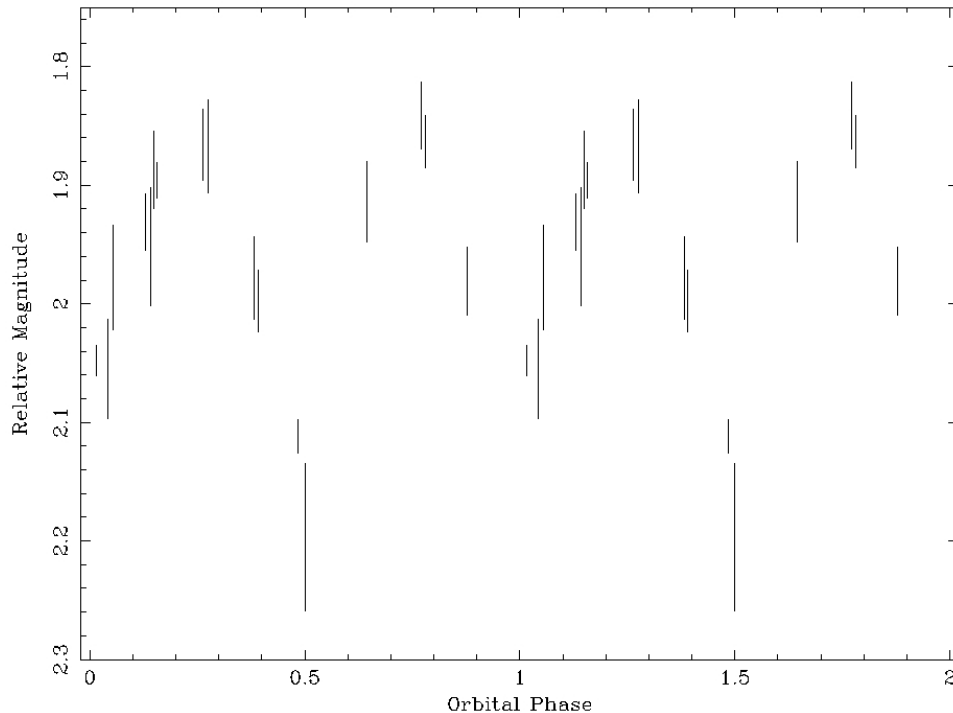
Figure 4.5: The ellipsoidal variability of GRO J1655–40 during May–June 1998.

4.1.3 Obtaining the Apparent Magnitudes

We next calculated the apparent magnitude of the system. We did this by photometricly calibrating our data. (See § 2.4.8 on page 33 for more details.)

CTIO CIRIM Images

We first attempted to calibrate the images using the observations made with the CTIO CIRIM detector. Previously Curran (2001) calculated the number of counts per second for a star of 10th magnitude (f_{10}) for the CTIO CIRIM detected. These values were:

$$f_{10}(J) = 10,900 \pm 400 \, \text{counts/sec}, \tag{4.1}$$

$$f_{10}(K_s) = 6580 \pm 80 \, \text{counts/sec}.$$

The log of the 1998 observations was consulted to determine which of the original images were taken during photometric conditions. One grid of such images
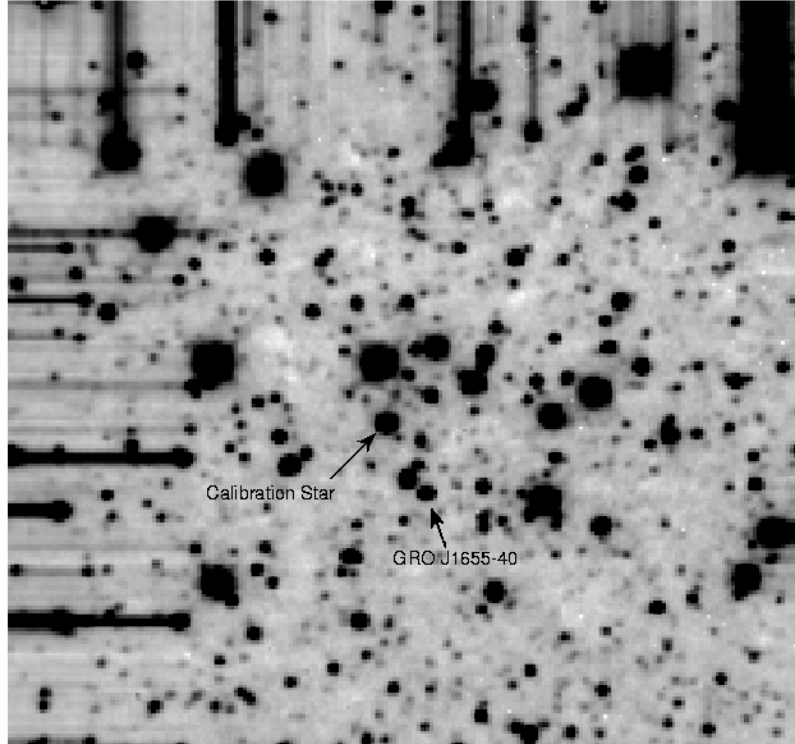
Figure 4.6: The selected photometric image from the 1998 K_s data, with the target star and calibration star indicated. This 30 second exposure, with a field of view of $\sim 166'' \times 166''$, was obtained using the CTIO CIRIM detector during June 1998.

was selected and aperture photometry was performed on the combined image of this grid. The chosen image is shown in Figure 4.6, and the calibration star is marked.

Table 4.2: Apparent Magnitude of Calibration Star

J Apparent Magnitude (mag)	K_s Apparent Magnitude (mag)
12.81 ± 0.05	11.29 ± 0.05

The magnitudes of the comparison star in each filter are given in Table 4.2.

Using these calibration magnitudes, the K_s–band and J–band magnitude of GRO J1655–40 were calculated as described in § 2.4.8. These values are listed

Table 4.3: Initial GRO J1655–40 Apparent Magnitudes

Year	J Apparent Magnitude (mag)	K_s Apparent Magnitude (mag)
1995	12.71 ± 0.05	11.98 ± 0.05
1998	13.81 ± 0.05	13.00 ± 0.05

in Table 4.3. The magnitudes calculated from the 1998 data were taken as the quiescent magnitudes of GRO J1655–40, whereas the 1995 magnitudes were taken to be outburst magnitudes (see § 3.2.2). It can be immediately seen that the system was brighter during outburst by approximately one magnitude.

KECK SCAM Images

The second calibration was performed using the KECK observations of GRO J1655–40. Although these observations were not made under ideal photometric conditions, it was hoped that these images would provide a check for the earlier calibration.

During a KECK SCAM observation run prior to our run in 2000, the value of f_{10} was determined to be approximately 400,000 counts per second (Callanan 2001). We applied aperture photometry to the calibration star in the KECK images to measure the count rate f of this star. Figure 4.7 on the next page shows the processed KECK image with the calibration star indicated. The apparent $K-$ band magnitude, K, of the star was then determined to be 11.25 ± 0.05 mag. The apparent K magnitude of GRO J1655–40 was then calculated, and found to be 12.95 ± 0.05 mag. This value was consistent with the preceding measurement using the 1998 CTIO images[2], validating the calibration.

2MASS All-Sky Point Source Catalog

During the preparation of this thesis, the **All-Sky Point Source Catalog (PSC)** from the **Two Micron All Sky Survey (2MASS)**[3] was released. We decided to verify our calibration of GRO J1655–40 using this more reliable source.

---

[2]We take the magnitude of the star in the $K-$ and K_s–bands to be equal.

[3] `http://irsa.ipac.caltech.edu/`
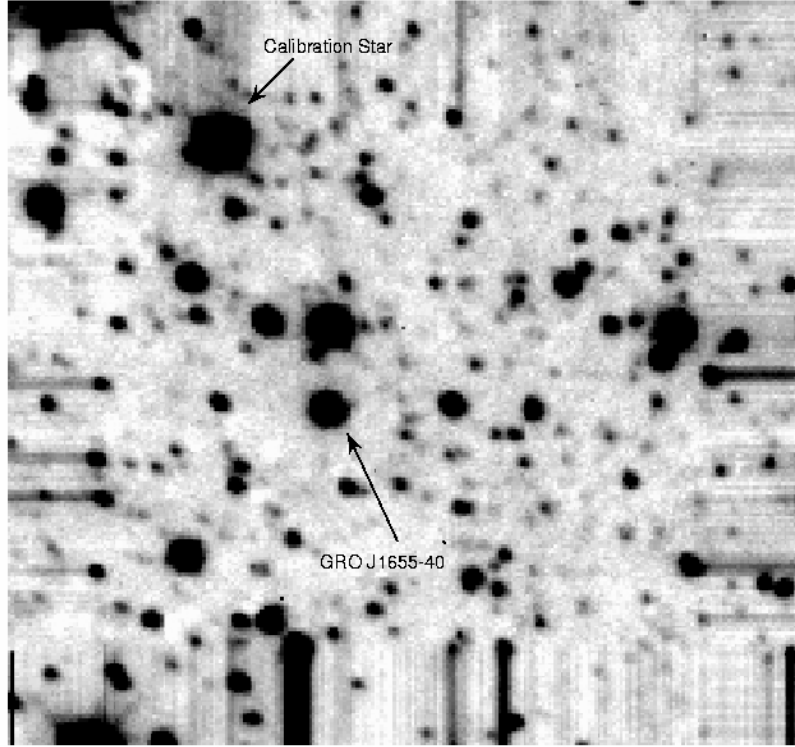
Figure 4.7: The field of view for the KECK images. The target star and the calibration star are marked. This $\sim 46'' \times 46''$ image was obtained with a 1×10 second exposure using the KECK S-CAM detector during June 1998.

Table 4.4: 2MASS Apparent Magnitudes

Source	J Apparent Magnitude (mag)	K_s Apparent Magnitude (mag)
GRO J1655–40 [a]	13.516 ± 0.029	12.744 ± 0.034
Calibration Star	12.757 ± 0.029	11.153 ± 0.021

[a]At Phase 0.21.

First, we obtained the apparent magnitudes of both our calibration star and GRO J1655–40 from the PSC – see Table 4.4 for these values. (We noted that the Modified Julian Date of the 2MASS observation of GRO J1655–40 was 51309.7443, which corresponds to an orbital phase of approximately 0.21.)

.

Table 4.5: GRO J1655–40 Apparent Magnitudes

Year	J Apparent Magnitude (mag)	K_s Apparent Magnitude (mag)
1995	12.77 ± 0.03	11.83 ± 0.04
1998	13.76 ± 0.03	12.86 ± 0.02

As there was a slight discrepancy between our CTIO measurement of our calibration star and the values from 2MASS, we decided to assume the 2MASS magnitudes for the calibration star, due to the extra reliability of this source. We then used these values to calculate the apparent magnitude of GRO J1655–40 in both the J– and K_s–bands. These magnitudes are listed in Table 4.5.

Table 4.6: Apparent Magnitude of GRO J1655–40

Source	J (mag)	K (mag)
Our 1998 K_s–band Data	13.76 ± 0.03	12.86 ± 0.02
Greene, Bailyn, & Orosz (2001)	13.85 ± 0.02	13.25 ± 0.02
Beer & Podsiadlowski (2002) (predicted)	13.8	13.0

Our values for the apparent magnitude of GRO J1655–40 during quiescence were then compared to prior estimates, listed in Table 4.6. Although our J–band value coincides with the two other values, there is a 0.4 magnitude disagreement between our K–band value and that of Greene, Bailyn, & Orosz (2001). A similar discrepancy has already been noted by Beer & Podsiadlowski (2002), who obtained a theoretical magnitude in better agreement with our own. This suggests our result is valid, although why the discrepancy between Greene, Bailyn, & Orosz (2001) and ourselves exists is unclear.

4.1.4 The Dereddened Magnitudes

We then corrected this magnitude to account for interstellar extinction. We obtained a value for the reddening, E_{B-V}, for GRO J1655–40 from Hynes et al. (1998):

$$E_{B-V} = 1.2 \pm 0.1 \text{ mag.} \tag{4.2}$$

We derived the $K-$ and $J-$band extinction following the discussion on page 34, and obtained the values of $A_K = 0.42\pm0.04$ mag and $A_J = 1.05\pm0.09$ mag. (Note that the values for interstellar extinction in the infrared is much lower than that in the optical, which is given by $A_V = 1.3 \times 3.1 = 4.0\pm0.3$ mag. This is as expected – see § 2.3 on page 27.) The **dereddened magnitudes** of GRO J1655–40 in the $J-$ and $K-$band were then calculated, and are summarised in Table 4.7. The difference of 1 mag between both the two values for K_0 and those for J_0 were attributed to the contribution from the disk during the outburst in 1995.

Table 4.7: Dereddened J, K and $J - K$ Magnitudes for 1995 and 1998

Year	J_0 (mag)	K_0 (mag)	$J_0 - K_0$ (mag)
1995	11.72 ± 0.09	11.41 ± 0.06	0.3 ± 0.1
1998	12.71 ± 0.09	12.44 ± 0.04	0.3 ± 0.1

Using the derived values of K_0 and J_0, we calculated the dereddened $J - K$ colour of GRO J1655–40 for 1995 and 1998. These values are also given in Table 4.7.

Table 4.8: Comparison Dereddened Magnitudes

Source	J_0 (mag)	K_0 (mag)	$J_0 - K_0$ (mag)
Greene, Bailyn, & Orosz (2001)	12.80 ± 0.09	12.83 ± 0.04	0.0 ± 0.1
Beer & Podsiadlowski (2002)[a]	12.75	12.58	0.17

[a]From their predicted apparent magnitudes.

Finally, we calculated the dereddened magnitudes using the apparent magnitudes calculated by Greene, Bailyn, & Orosz (2001) and those predicted by Beer & Podsiadlowski (2002). Table 4.8 lists these values. Again, our value for $J_0 - K_0$ during quiescence is in good agreement with that predicted by Beer & Podsiadlowski (2002), but differs from that of Greene, Bailyn, & Orosz (2001). It should however be noted that in general $J_0 - K_0 > 0$, which supports our earlier conclusion that the K magnitude derived by Greene, Bailyn, & Orosz (2001) may be erroneous.

According to Beer & Podsiadlowski (2002), the spectral type of GRO J1655–40 lies within the range F5–G0 III–IV. We compared our dereddened $J - K$ with that of UKIRT standard stars with a spectral type similar to GRO J1655–40. We found that the value $J_0 - K_0 = 0.3\,\mathrm{mag}$ was consistent with a spectral type of F0–G2 III–IV, which is in agreement with, if not as precise as, the spectral range of Beer & Podsiadlowski (2002).

4.1.5   The Absolute Magnitudes

As a final check for self-consistency in our derived value for the magnitude of GRO J1655–40, we calculated the absolute $J-$ and $K-$magnitudes of this system using Equations 2.5 and 2.6. We assumed a distance of 3.2 kpc for this calculation (Hjellming & Rupen 1995). These magnitudes are tabulated in Table 4.9.

Table 4.9: J and K Absolute Magnitudes of GRO J1655–40

Year	M_J (mag)	M_K (mag)
1995	-0.8 ± 0.2	-1.1 ± 0.2
1998	0.2 ± 0.2	-0.1 ± 0.2

We then compared the absolute magnitudes from 1998 with the quiescent absolute magnitudes of several other SXTs, namely GRS 1121–68, A0620–00 and V404 Cyg, some of the properties of which are given in Table 4.10 on the following page. We consulted the literature for the relevant J and K magnitudes and the interstellar reddening of these systems, and calculated the absolute magnitude of each. Table 4.11 on page 59 lists the derived absolute magnitudes.

The absolute magnitude of GRO J1655–40 is more consistent with that of V404 Cyg, a result which is to be expected as both systems are long period binaries, whereas the other SXTs are short period systems.

Table 4.10: Periods and Distances of Comparison SXTs

	P	d (kpc)
GRS 1121–68	$10\overset{\text{h}}{.}5^{a}$	2.8^{b}
A0620–00	$7\overset{\text{h}}{.}75^{c}$	1^{d}
V404 Cyg	$6\overset{\text{d}}{.}5^{e}$	3.5^{f}

[a]Bailyn (1992).
[b]Shahbaz et al. (1997).
[c]Froning & Robinson (2001).
[d]Elvis et al. (1975).
[e]Casares, Charles, & Naylor (1992).
[f]Shahbaz et al. (1994).

4.2   Modelling the Light Curve of GRO J1655–40

In this chapter, we have demonstrated how we obtained a measure of the ellipsoidal variability of GRO J1655–40 during quiescence. In the next chapter, we will explain how we employed numerical simulations of this light curve to obtain a value for the mass ratio q and the binary inclination i of our target system.

Table 4.11: Absolute Magnitudes of SXTs

	J (mag)	A_J (mag)	M_J (mag)
GRS 1121–68	17.5[a]	0.35[a]	4.99[a]
A0620–00	15.6[b]	0.31[c]	5.29
	K (mag)	A_K (mag)	M_K (mag)
GRS 1121–68	16.7[c]	0.14[c]	4.33[c]
A0620–00	14.5[c]	0.12[c]	4.38
V404 Cyg	12.4[d]	0.32[e]	-0.64

[a]Chaty et al. (2002).

[b]Froning & Robinson (2001).

[c]Calculated using $E_{B-V} = 0.35$ mag (van Paradijs & McClintock 1995).

[d]Shahbaz et al. (1994).

[e]Computed using $A_V = 2.8$ (Shahbaz et al. 1994).

Chapter 5

The Eclipsing Light Curve Code

Having obtained the light curve of GRO J1655–40, we attempted to model the data through numerical simulations of the X–ray binary. Here we outline the components of the model, and discuss the values obtained for the mass ratio and inclination.

5.1 Introduction to *ELC*

The **Eclipsing Light Curve** (*ELC*) code[1] was written by Jerome A. Orosz, of the Universiteit Utrecht in the Netherlands[2]. This suite of programs creates a theoretical model of a star system, based on a user-specified set of parameters, such as the mass ratio and orbital inclination of a binary system. It then modifies the light curve until it obtains the best fit to the observations of the user.

The *ELC* programs can model the light curve of:

- **a binary star system**: for example, an X–ray binary, where the companion star is denoted by star 1 and the compact star by star 2.

- **a binary system with an accretion disk**, such as an X–ray binary with a disk around the compact object (star 2).

---

[1] We ran version 2 of this program, as described by the author in Orosz & Hauschildt (2000)

[2] The author is now in San Diego State University.

The component stars can have eccentric orbits, and the effect of mutual eclipses of the accretion disk and secondary star can be included in the model.

The three *ELC* programs that were employed in our modelling were:

- `ELC`[3], which creates light curve models (in linear units) for several passbands based on a list of system parameters.

- `gridELC`, an optimizer based on the "grid search" routine (Bevington 1969). Given a series of folded light curves and radial velocity curves, `gridELC` will adjust user-specified parameters to find the minimum χ^2 of the fit of the *ELC* model to the data. The final set of parameters are then used to create light curve models (in linear units).

- `checkfit`, which converts the linear `gridELC` model to magnitudes and then scales it according to the data.

We utilised these *ELC* programs to model both the 1998 and 1995 data sets.

5.2 The 1998 K_s–band Data

5.2.1 Details of the Quiescent Model

The quiescent observations of GRO J1655–40 were modelled by accounting only for the ellipsoidal variability of the secondary star. The disk contribution to the overall flux of the system was assumed to be negligible (we will later show this to be a valid assumption – see § 6.1.4 on page 74), and hence we assumed there would be no noticeable eclipse of the accretion disk. It was also assumed that there was no X–ray heating of the secondary star. The model we employed was of a binary system with a Roche lobe filling secondary star and a black hole primary star.

---

[3] Note that the abbreviation ELC can refer to either the suite of programs (referred to in this text by the use of italics: *ELC*) or this specific program (referred to by using typewriter font: `ELC`).

5.2.2 Modelling Procedure for the 1998 Data

The following procedure details how we modelled the 1998 observations of GRO J1655–40 using the described model.

- We obtained a folded light curve for the 1998 K_s–band observations (see § 4.1.2 on page 48). This light curve was phased according to the convention of Orosz & Bailyn (1997) which places star 1 (with filled Roche lobe) in front of the compact star 2 at phase 0.0. See Figure 4.5 on page 51 for the plot of this light curve.

- The literature was consulted for values of the parameters in Table 5.1 on page 69. The values for the parameters in Table 5.2 on page 69 were set from experience.

- Since this model ignored X–ray heating and the accretion disk, the parameters in Table 5.3 on page 70 were set to the appropriate values.

- `ELC` was run without a input file to produce a **parameter file** with each parameter set to its default value. This file was edited, setting the parameters to the values shown in Tables 5.1–5.3. The remaining parameters were left at their default values.

- `ELC` was run once more, this time using the **edited** input file. This created a model binary system based on the values given for the system parameters, and outputted this in both linear and magnitude units to a data file.

- The parameter file for `gridELC` was edited, to specify both the folded light curve data file and the parameters to be adjusted, namely the mass ratio and inclination.

- `gridELC` was run. The final values calculated for the adjusted parameters were noted.

- The χ^2 value of the fit of the model to the observations was determined

using `checkfit`, from which the reduced chi-squared[4] was calculated.

- The resultant model plot and the light curve data were superimposed for a visual check of the fit.

5.2.3   Comparison of Quiescent Model and Results
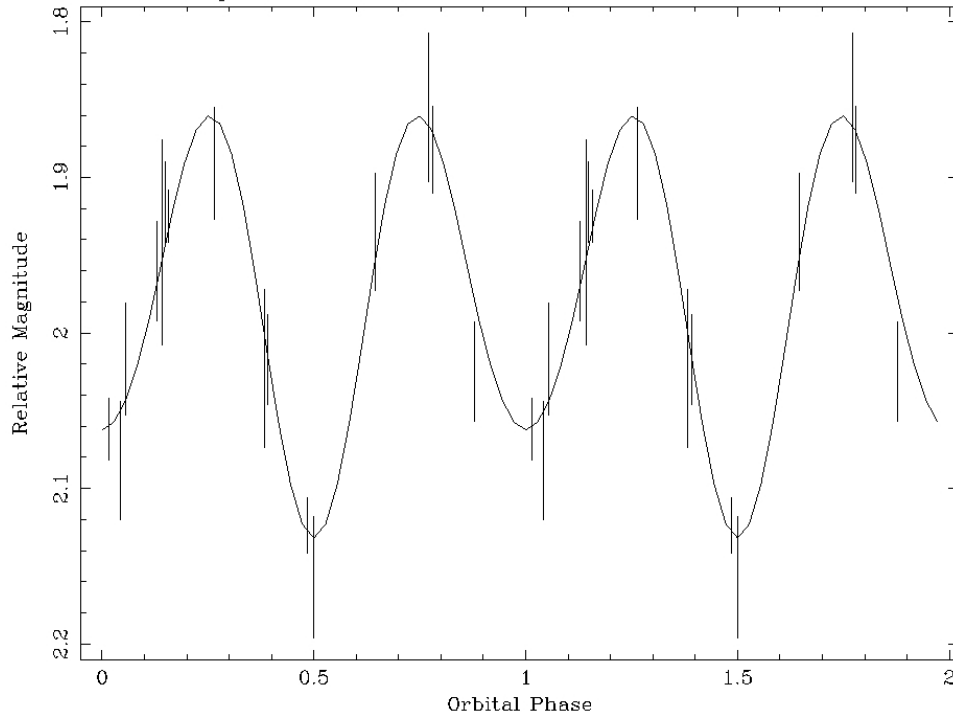
Figure 5.1: The observed K_s light curve for GRO J1655–40 in May/June 1998, together with a theoretical light curve computed for a mass ratio of 2 and a binary inclination of 69°. Two orbital cycles are shown for clarity.

As can be seen in Figure 5.1, the data were well modelled by our theoretical

---

[4] The reduced chi-squared (χ^2_ν) of the fit is defined by:

$$\chi^2_\nu = \frac{\chi^2}{n - p - 1},$$

where n is the number of the data points and p is the number of parameters of the fit. A χ^2_ν value of approximately 1 was desired.

light curve, and we obtained $\chi_\nu^2 = 0.51$ as the reduced chi-squared[5]. The theoretical light curve mimics the ellipsoidal variability of the secondary, with the expected deeper minimum at phase 0.5.

Derived Mass Ratio and Inclination
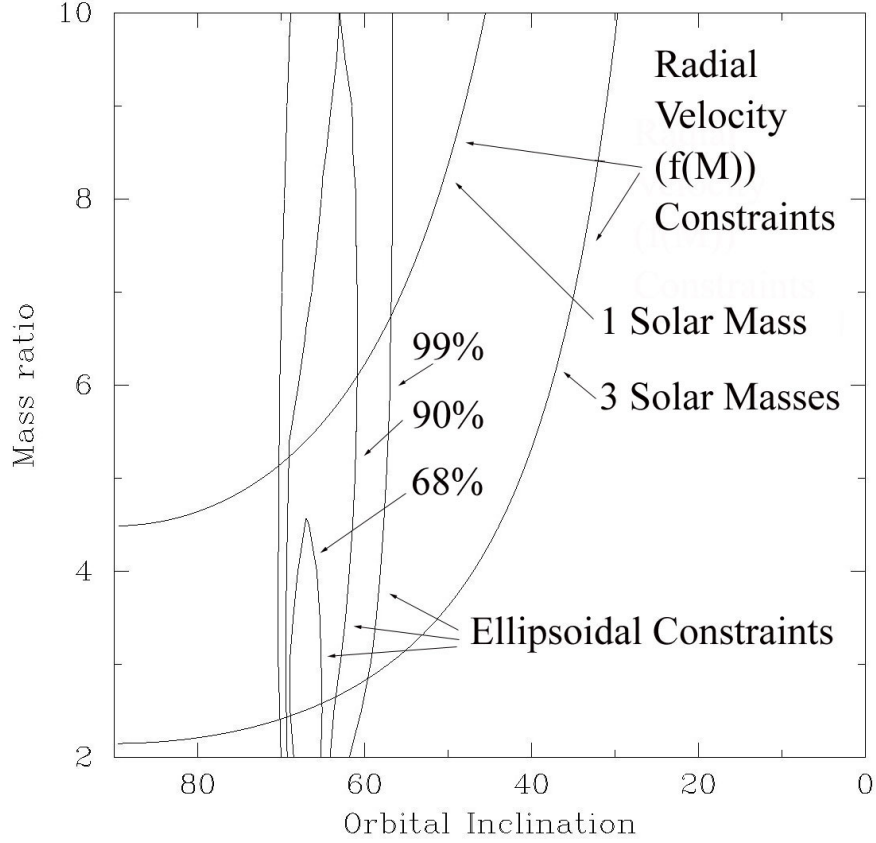
Figure 5.2: The χ^2 contour plot for the 1998 K_s–band data. This plot displays the 68%, 90% and 99% confidence levels from the `ELC` fits, together with constraint curves derived from the mass function assuming a secondary mass of $1\,M_\odot$ and $3\,M_\odot$, respectively. (The minimum reduced χ^2 has been set equal to 1.)

In order to properly constrain the mass ratio and the inclination, `gridELC` was run to create a χ^2 contour plot. We simultaneously varied the inclination

---

[5] We interpret this low χ_ν^2 value as signifying that `DAOPHOT` is overestimating the errors for the estimates of the relative magnitude of GRO J1655–40.

between $i = 0°$ and $i = 90°$ and the mass ratio between $q = 2$ and $q = 10$, and computed the χ^2 of the fit using `gridELC`. Figure 5.2 on the previous page shows the resultant plot, together with constraints for i and q derived from the mass function and secondary mass considerations, assuming (conservatively) that the mass of the secondary lies between $1\,M_\odot$ and $3\,M_\odot$– it is an F/G (sub)giant. The area in Figure 5.2 where the mass function and ellipsoidal modelling constraints overlap denotes the allowed values of q and i. Generally, our results show that the inclination of the system lies in the range $i = 64°$–$70°$, and that the mass ratio lies in the range $q = 2.5$–6, at the 90% confidence level.

Table 5.4 on page 70 compares the values we derived for the mass ratio q and the inclination i of GRO J1655–40 with those from other studies of this system. From this table, it can be seen that the values for both our mass ratio and orbital inclination are consistent with past estimates.

Derived Component Masses

Using our values for q from the 1998 data ($q = 2.5$–6) and the corresponding secondary masses ($M_2 = 1$–$3\,M_\odot$), we derived the mass of the primary as $6.8 \pm 0.7\,M_\odot$. This is to be compared in particular with the results from the only other infrared study of this system, which yielded $M_X = 6.3 \pm 0.5\,M_\odot$ (Greene, Bailyn, & Orosz 2001). Table 5.5 on page 70 compares this mass with masses from earlier studies.

Our values are consistent with preceding results, and is above the standard limit for neutron star masses. This implies that the compact object in GRO J1655–40 is a black hole, if we accept the neutron star mass limit of Rhoades & Ruffini (1974). We note however that this result is dependent on the assumption of negligible disk contamination.

5.3 The 1995 K_s–band Data

5.3.1 Details of Outburst Model

The model for the outburst of GRO J1655–40 included: (i) the ellipsoidal variability of the Roche lobe filling secondary, (ii) a bright hot accretion disk and (iii) eclipses of the accretion disk and the secondary.

5.3.2 Modelling Procedure for the 1995 Data

The procedure for modelling the 1995 K_s observations was essentially the same as for the 1998 data. Here, we outline the main differences:

- The variable parameters were set as to include an accretion disk and eclipses – see Table 5.6 on page 71.

- Rather than attempting to vary the mass ratio and inclination, we fixed these parameters to the values obtained from the quiescent data, and applied these values in our attempt to fit the outburst data.

5.3.3 A Poor Fit

Figure 5.3 on the following page shows the resultant fit of our model to the outburst data. We obtained a reduced chi-squared of $\chi^2_\nu = 5.89$. The fit is much poorer than for the 1998 data, for the reasons we now outline.

The Accretion Disk

Since GRO J1655–40 was in outburst at the time of these observations, the flux from the accretion disk was more significant than the ellipsoidal variability of the secondary star. The deeper minimum at phase 0 is indicative of an eclipse of the bright accretion disk by the secondary star. The presence of eclipses agrees well with the high orbital inclination of this system.

We note that there is no evidence of an eclipse of the accretion disk in the quiescent light curve, even though GRO J1655–40 has been shown to be an eclipsing binary from the outburst observations, and in spite of the high inclination
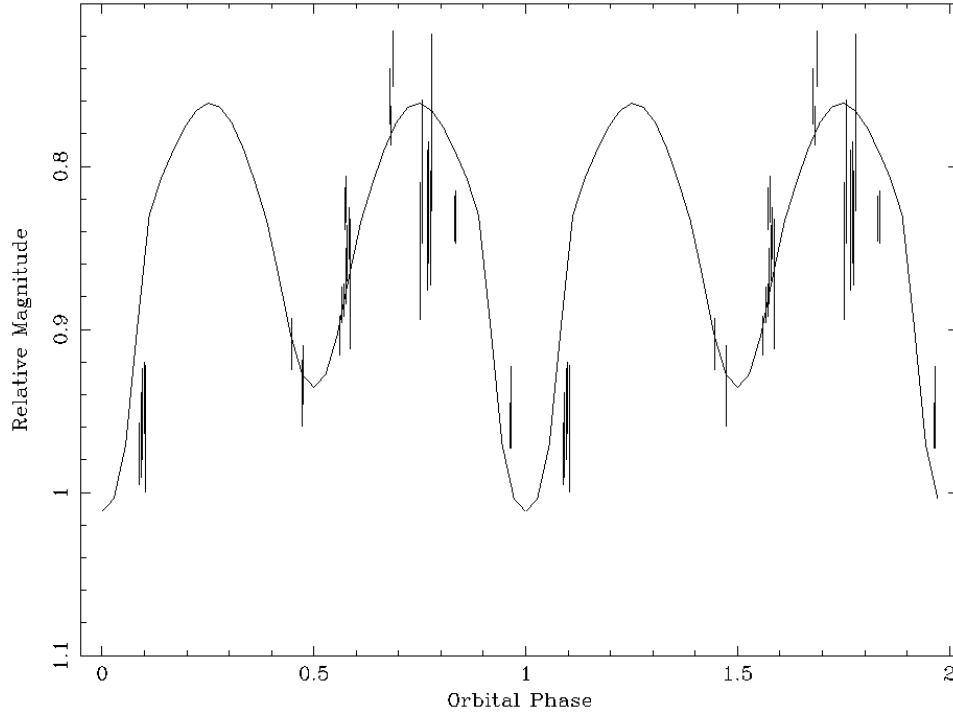
Figure 5.3: The June 1995 K_s light curve of GRO J1655–40, with a model light curve using the mass ratio and inclination from the best fits of the 1998 data set ($q = 2$, $i = 69°$).

($i \sim 70°$) of the system. This is consistent with the negligible disk contribution to the overall flux from the system during quiescence.

The reduced χ^2 values obtained for the outburst data are significantly higher than the quiescent values. One possible explanation for this is that the accretion disk is significantly non-axisymmetric, or exhibits infrared flaring or flickering activity, which the code is unable to account for. Orosz & Bailyn (1997) were also unable to accurately model their optical outburst data, taken during August 1994 and March–April 1995, and obtained larger reduced χ^2 values from modelling their outburst data than from their quiescent data.

5.4   Does the Accretion Disk Contribute?

Although we have now obtained a plausible value for the mass of the black hole in GRO J1655–40, we made the assumption that the contribution of the accretion disk in the infrared was negligible. In the following chapter, we explain how we confirmed this assumption from infrared spectroscopy of the binary system.

Table 5.1: Fixed *ELC* Binary System Parameters

Name	Description	Value
Q	Mass ratio	3.9^a
finc	Inclination	$68°65^a$
Tgrav1	Gravity Darkening exponent, star 1	0.25^b
Period	Orbital period of binary	$2\overset{\text{d}}{.}62168^b$
betarim	Angle of disk to orbital plane	$\sim 2°\,^c$
alb1	Bolometric albedo, star 1	0.5^c
fm	Mass function, star 2	$2.73\,\mathrm{M_\odot}{}^d$
separ	Orbital separation	$\sim 16\,\mathrm{R_\odot}{}^d$
Teff1	Mean temperature, star 1	$\sim 6400\,\mathrm{K}^e$
Teff2	Mean temperature, star 2	$< 0\,\mathrm{K}^f$
fill1	Roche lobe filling factor, star 1	1.000^g
fill2	Roche lobe filling factor, star 2	0.000^h
eccen	Eccentricity of orbit	0^i
omega1	Ratio of rotational to orbital frequency, star 1	1^i
omega2	Ratio of rotational to orbital frequency, star 2	1^i

[a]Beer & Podsiadlowski (2001) – these values were only initially fixed.
[b]van der Hooft et al. (1998).
[c]Orosz & Bailyn (1997).
[d]Shahbaz et al. (1999).
[e]Corresponding to a star of spectral type F5–G0 III–IV (Beer & Podsiadlowski 2001).
[f]*ELC* interprets this to mean that the primary star is an invisible black hole.
[g]Since accretion continues in quiescence (see § 1.3.7 on page 15).
[h] Primary star is a black hole.
[i]This close binary should have synchronously rotating components in a circular orbit.

Table 5.2: Fixed *ELC* Parameters

Name	Description	Value
Nalph1, Nalph2	Number of latitude grid elements	100
Nbet1, Nbet2	Number of longitude grid elements	35
Ntheta	Number of azmithual grid points	90
Nradius	Number of radial grid points	80
ilaw	Controls form of limb darkening law	1 (Linear law)

Table 5.3: Values of Variable *ELC* Parameters for 1998 Data

Name	Description	Value
iecheck	Switch for eclipses	-1[a]
idint	Switch for disk	0[b]
rinner	Inner radius of disk	_[b]
router	Outer radius of disk	_[b]
xi	Power-law exponent on the disk temperature profile	_[b]
tdisk	Temperature of inner disk	_[b]
Nref	Number of iterations for reflection effect	0[c]
Lx	$\log_{10} L_X$ for primary star in X–ray binary	0[c]

[a]No eclipses.
[b]No disk present.
[c]No X–ray heating.

Table 5.4: Comparison of Derived Values for q and i

Data Set	q	i
Our 1998 K_s–band Data	$2.5 - 6$	$64° - 70°$
Beer & Podsiadlowski (2002) (Predicted)	3.9 ± 0.6	$68°\!.65 \pm 1°\!.5$
Greene, Bailyn, & Orosz (2001)	2.6 ± 0.3	$70°\!.2 \pm 1°\!.9$
Shahbaz et al. (1999)	2.29–2.97	–
van der Hooft et al. (1998)	2.43–4.20	$63°\!.7$–$70°\!.7$
Orosz & Bailyn (1997)	2.99 ± 0.08	$69°\!.50 \pm 0°\!.08$

Table 5.5: Comparison of Derived Values for M_X

Data Set	M_X (M$_\odot$)
Our 1998 K_s–band Data	6.8 ± 0.7
Beer & Podsiadlowski (2002) (Predicted)	5.4 ± 0.3
Greene, Bailyn, & Orosz (2001)	6.3 ± 0.5
Shahbaz et al. (1999)	5.5–7.9
van der Hooft et al. (1998)	6.29–7.20
Orosz & Bailyn (1997)	7.02 ± 0.22

Table 5.6: Values of Variable *ELC* Parameters for 1995 Data Set

Name	Value
iecheck	0^a
idint	1^b
rinner	0.55
router	1.0
xi	-0.8^c
tdisk	$\sim 13000\,\mathrm{K}$
Nref	0^d
Lx	0^d

[a]Check for eclipses.

[b]Accretion disk present.

[c]Assuming a steady-state disk.

[d]No X–ray heating.

Chapter 6

The Accretion Disk Contamination

Although we have now obtained a value for the mass of the black hole in GRO J1655–40, this is not be a reliable estimate, unless we first confirm that the disk contamination is negligible in this system. Here we discuss the application of infrared spectroscopic techniques to determine from the spectral features of GRO J1655–40 the contribution of the accretion disk.

6.1 Spectroscopy of GRO J1655–40

We processed the NIRSPEC data as follows to obtain spectra from which we could accurately measure the absorption and emission features present in the spectrum of GRO J1655–40.

6.1.1 The Initial Reduction

We first subtracted the background from the spectra of our target GRO J1655–40, and also for the spectra of HD 326320, an A0 star (see page 44), as outlined in § 2.5.1.

The gain and read noise for the NIRSPEC detector were obtained from the

instrument webpage[1]. 1-D spectra were then extracted from the background subtracted images, using these parameter values in *apall*. (See § 2.5.2 for details.)

A dispersion correction was calculated and applied to the spectra using the `identify` and `reidentify` tasks: (i) We obtained an Argon arc lamp map from the webpage[2] of the UKIRT CGS4 detector, containing accurate wavelengths of numerous spectral lines. (ii) These lines were marked on one of the extracted Ar arc spectra. (iii) The corresponding vacuum wavelengths were entered into the `identify` database. (iv) A cubic spline function was fitted to these data. (v) Significantly bad data points were identified and removed, and a new fit was applied, with a rms of 1.6 Å. (vi) The function was then applied to identify the spectral lines in the other extracted arc spectra, using the task `reidentify`.

Each of the spectra of GRO J1655–40 and HD 326320 was then assigned one of the arc spectra using `refspectra`. The cubic fits calculated from `identify` and `reidentify` were used by `dispcor` to dispersion correct the extracted target spectra.

The wavelength-callibrated spectra were then normalised by using the task `continuum` to fit the continuum of each spectrum to a spline of order 2.

6.1.2 Removing the Telluric Features

Having obtained normalised spectra of our system, we next removed the features in the spectra that were due to atmospheric absorption (see § 2.5.5). We had chosen the A0-type star HD 326320 to act as our comparison star, due to the scarcity of prominent features in the K–band. We masked the only major feature (Br-γ) in the comparison star spectra, and the target star spectra were then divided by the resultant spectrum.
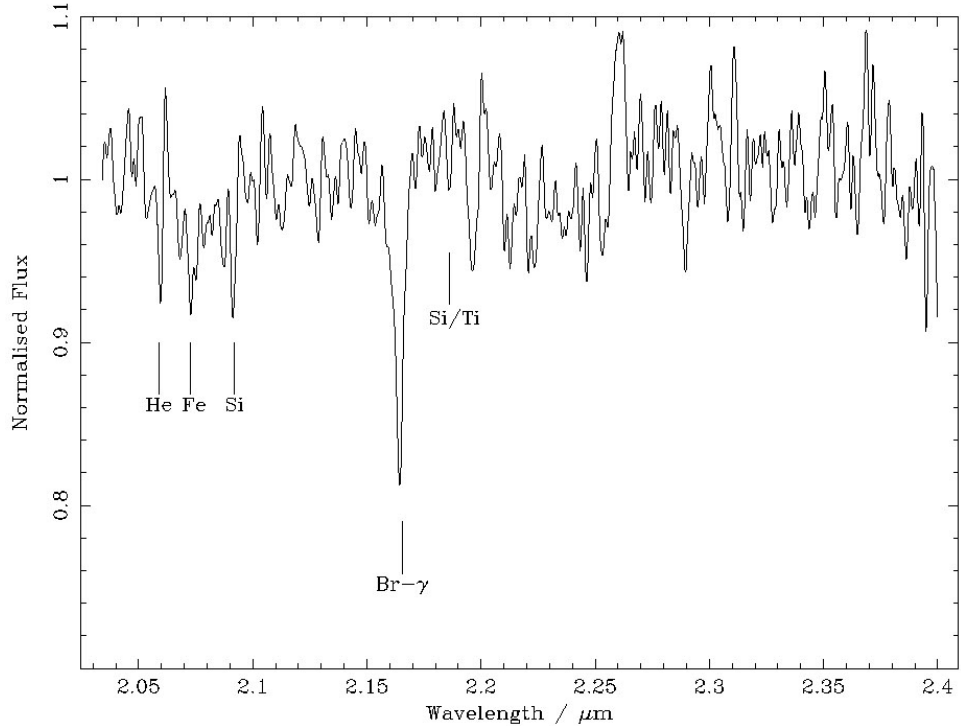
Figure 6.1: The *K*–band spectrum of GRO J1655–40, having been corrected for telluric features with reference to an A0 star. The dominant Br-γ feature is marked, together with several weaker features.

6.1.3   Our Spectrum of GRO J1655–40

The final spectrum was obtained by combining the two corrected target spectra, and smoothing the resultant spectrum, as we explained in § 2.5.6. Our spectrum of GRO J1655–40 is shown in Figure 6.1.

6.1.4   Determining the Disk Contribution

In order to determine the degree of accretion disk contamination in GRO J1655–40, we compared our spectrum of this system with spectra of isolated stars of similar spectral type to the secondary in GRO J1655–40. We obtained these comparison spectra from the literature, and calculated the equivalent width (see § 2.2.1 on page 24) of the Br-γ absorption feature in the target and comparison spectra. If
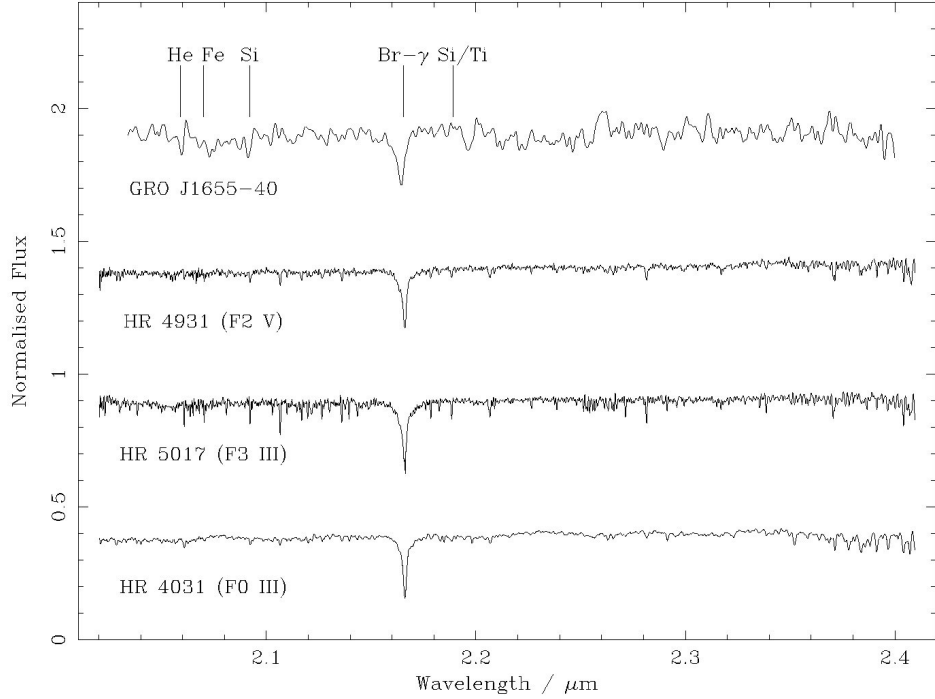
---

[1] `http://www2.keck.hawaii.edu:3636/realpublic/inst/nirspec/nirspec.html`

[2] `http://www.jach.hawaii.edu/JACpublic/UKIRT/instruments/cgs4/`

Figure 6.2: The K–band spectra of GRO J1655–40, HR 4031, HR 5017 and HR 4931, with the spectral features of interest marked.

the Br-γ feature in our spectrum of GRO J1655–40 was significantly weaker than the corresponding features in the sample spectra, this would imply that there was emission present in the K–band from the disk.

The isolated stars with spectral types of F5–G0 III–IV (the spectral type of GRO J1655–40: see Beer & Podsiadlowski 2002) were chosen from the spectral atlas of Wallace & Hinkle (1997). Figure 6.2 displays three of the chosen spectra[3], together with our spectrum of GRO J1655–40. The equivalent widths of the Br-γ absorption features in the telluric-corrected spectrum of GRO J1655–40 and the above stars were measured using `splot`. Table 6.1 on the next page lists these equivalent widths.

As can be clearly seen, the equivalent width for GRO J1655–40 agrees well

---

[3]The spectra were originally plotted with flux as a function of inverse wavenumber, but we converted them to μm for comparison with our spectrum.

Table 6.1: Equivalent widths of Br-γ feature

Identifier	Spectral Type	$W_\lambda/\text{Å}$	Identifier	Spectral Type	$W_\lambda/\text{Å}$
GRO J1655–40	F5–G0 III–IV	10 ± 1	HR 4931	F2 V	8 ± 1
HR 7495	F5 II–III	7.0 ± 0.5	HR 6927	F7 V	4.0 ± 0.5
HR 4031	F0 III	8.5 ± 0.5	HR 6608	G2 IIIb	3.0 ± 0.5
HR 5017	F3 III	8 ± 1	HR 7373	G8 IV	3 ± 1
HR 21	F2 IV	7 ± 1	HR 4375	G0 V	3 ± 1
HR 8905	F8 IV	4.5 ± 0.5	HR 483	G1.5 V	3.5 ± 0.5
HR 2943	F5 IV-V	6.5 ± 0.5	HR 7504	G3 V	3.0 ± 0.5

with certain stars, namely HR 4031, HR 5017 and HR 4931. This implies that the disk contributes little light to the system in the K–band, and also that the spectral type of the secondary star in GRO J1655–40 is within the range F5–F7 III–IV, which is consistent with our initial range of F0–G2 III–IV, derived in § 4.1.4 on page 55.

Table 6.2: Equivalent widths of weaker features

Identifier	He	Fe	Si	Si/Ti
GRO J1655–40	1.1 ± 0.2	0.8 ± 0.3	1.1 ± 0.2	0.5 ± 0.2
HR 4031	0.6 ± 0.1	0.4 ± 0.1	0.3 ± 0.1	0.4 ± 0.1
HR 5017	0.2 ± 0.1	0.6 ± 0.1	0.4 ± 0.1	0.5 ± 0.1
HR 4931	0.4 ± 0.2	0.5 ± 0.1	0.3 ± 0.1	0.3 ± 0.1

As well as comparing the equivalent widths of the Br-γ features in our spectra and those of Wallace & Hinkle (1997), we also compared the equivalent widths of weaker features that we could identify in these spectra. These were the He feature at $\lambda = 20\,590\,\text{Å}$, the Fe line at $\lambda = 20\,700\,\text{Å}$, the Si feature at $\lambda = 21\,360\,\text{Å}$ and the combined Si/Ti absorption at $\lambda = 21\,890\,\text{Å}$. The equivalent widths obtained are listed in Table 6.2.

Although the equivalent widths from the sample spectra are not in complete agreement with our results, there is at least no evidence of emission from the

disk, as the absorption features in our spectrum are stronger. We can therefore conclude that there is negligible disk contamination in GRO J1655–40 during quiescence. We compared our results with those of Israelian et al. (1999), who found that the atmosphere of GRO J1655–40 was similar to that of a standard F6–F7 III–IV star, with an almost solar Fe abundance. They did find, however, an overabundance of α–elements, such as Si and Ti. Our results support these conclusions.

Hence, there is no evidence of emission from the disk, and we can conclude that there is negligible disk contamination in GRO J1655–40 during quiescence.

6.1.5 Calculating the Radial Velocity

As a check for consistency, we calculated the radial velocity of the secondary star in GRO J1655–40 from the published spectroscopic ephemeris during the time of the observation, and compared this theoretical value with that derived from our spectra of this system.

We first determined from the Universal Date and Time of the observation of GRO J1655–40 and using the ephemeris of van der Hooft et al. (1998) that the system was at phase 0.05. Using the values for γ and K_2 from Orosz & Bailyn (1997), namely:

$$\gamma = -142.4 \pm 1.6 \, \mathrm{km \, s^{-1}}, \tag{6.1}$$

$$K_2 = 228.2 \pm 2.2 \, \mathrm{km \, s^{-1}}, \tag{6.2}$$

we determined that the radial velocity of the secondary at phase 0.05 should be $v_r = -142 \pm 2 \, \mathrm{km \, s^{-1}}$.

From our telluric-corrected spectrum of GRO J1655–40, we determined the wavelength of the Br-γ feature to be $\lambda_{\mathrm{obs}} = 21\,644.41 \, \text{Å}$. Using Equation 2.11 on page 26, we calculated that the corresponding radial velocity of the secondary star is $v_r = -147 \pm 5 \, \mathrm{km \, s^{-1}}$. We therefore conclude that the Doppler shift of the spectral features of the secondary star due to its radial velocity are as expected.

6.2 Negligible Disk Contamination!

Having confirmed that GRO J1655–40 was indeed in quiescence during our observations in 1998, with little contribution from the accretion disk to the total flux from the binary, we can have confidence in our derived value for the mass ratio, the inclination and most importantly the mass of the black hole.

Chapter 7

General Conclusions

The most significant finding in this thesis is that the accretion disk in GRO J1655–40 contributes negligible flux during quiescence to the overall system flux in the K–band. The spectrum of GRO J1655–40 is similar to that of an isolated F5–F7 III–IV star. We can therefore justify modelling the K–band quiescent observations of GRO J1655–40 by only considering the ellipsoidal variability of the secondary star, and can rely on the derived values for the mass ratio and inclination.

From such modelling of GRO J1655–40 during quiescence, we have derived values for the mass ratio and inclination of this system of 2.5–6 and 64°–70°, respectively, which are in good agreement with prior results. As the disk contamination has been shown to be negligible, the value for the orbital inclination can be taken as a valid estimate. We can therefore conclude that the primary star in GRO J1655–40 is a black hole candidate, with a mass of $M_X = 6.8 \pm 0.7\,\mathrm{M_\odot}$.

From our attempts to model GRO J1655–40 in outburst, we have determined that the ELC model employed is too simplistic for an adequate fit to the observations of binary system with an asymmetric bright disk. The code is, however, able to model the eclipsing of the disk, the presence of which is consistent with the inclination previously derived.

We have calculated the apparent magnitude of GRO J1655–40 in both the

J– and K_s–band. We find a $0.4\,\mathrm{mag}$ difference between our K_s–band result and that of Greene, Bailyn, & Orosz (2001). As we have determined that our colour estimate of $J_0 - K_0 = 0.3 \pm 0.1\,\mathrm{mag}$ is consistent with our spectral type for the secondary star in GRO J1655–40, we are in agreement with Beer & Podsiadlowski (2002) that there is an error in the value of Greene, Bailyn, & Orosz (2001).

Finally, we have confirmed that the quiescent absolute J and K magnitudes of this system ($0.2 \pm 0.2\,\mathrm{mag}$ and $-0.1 \pm 0.2\,\mathrm{mag}$, respectively) are as expected for a long period soft X–ray transient.

We have utilised the first high signal–to–noise K–band spectrum of a black hole X–ray transient system to confirm the absence of disk contamination in that system. Similar observations of other transient systems should be pursued in order to verify the mass of the compact objects already derived from observations of the ellipsoidal variability of these binaries. Further observations of SXTs in search of black hole candidates would also benefit from the use of ELC to model quiescent light curves.

Appendix A

IRAF

This appendix gives more specifics of the commands used for reduction and analysis. The parameters of some of the tasks are listed and discussed, and a description is given of the `DAOPHOT` procedure.

Further details about the `IRAF` tasks are available from the online `IRAF` help, accessed using the `help` task within `IRAF`, or from the user manuals for `IRAF` (Barnes 1993) and `DAOPHOT` (Davis 1994).

A.1   The Image Header

Each `IMH` image contains a series of text lines, known as the **image header**, in which the details of the observation are stored. The text serves as a digital copy of the observation log and is usually automatically added to the image at the observatory.

This information is accessed in `IRAF` by using the `imheader` task, e.g., `imheader` *image.imh longheader=yes*. The `hselect` command can alternatively be run to output information selectively from the header. This enables the user to rapidly identify relevant images based on various properties of the images. For example, the user can quickly identify all the images of a particular target star system.

Several important details usually included in the header are:

- The file name of the image.

- The location of the corresponding `IRAF` pixel file.

- The type of object was observed, whether it was a star, flatfield or arc.

- The name of the star or arc observed.

- The detector and telescope used.

- The slit employed for spectroscopic observations.

- The observatory where the observation was made.

- The name(s) of the observer(s).

- The filter band selected.

- The Universal Date and Time at which the observation of the frame began.

- The Universal Time at the end of the frame observation.

- The sidereal time of the observation.

- The integration time per coadd.

- The number of coadds.

- The right ascension and declination of the telescope.

- The airmass of the observation.

Depending on the detector used, other information may also be inserted into the header.

A.2 Photometry

A.2.1 Imexamine

The `imexamine` routine is run to extract information interactively from an image displayed in the `DS9` image viewer. A single image may be examined, or a list of

images. We used `imexamine` to perform aperture photometry on our images of
GRO J1655–40 as follows:

- We displayed an image using `DS9` and called the `imexamine` routine within
  IRAF.

- Next, we edited the parameters for `imexamine` while the task was running
  using the ":`epar`" cursor command. We activated logging and set the name
  of the log (*logfile*).

- We then set the *rimexamine* pset parameters (":`epar r`"). These are used
  during aperture photometry and include:

  radius Aperture radius for aperture photometry.

  magzero User defined zero point for magnitude scale. This value was
  determined from:

  $$\text{magzero} = 10 + 2.5 \log f_{10} I - k\chi, \tag{A.1}$$

  where f_{10} is the counts per second detected from a star of magnitude
  10, k is the extinction coefficient for the observatory, and I and χ
  are the total integration time and the airmass for the observation,
  respectively. Then the magnitude (m) of the star can be calculated by
  `imexamine` using:

  $$m = \text{magzero} - 2.5 \log_{10} F, \tag{A.2}$$

  where F is the counts from the star, measured by aperture photometry.

- Using the cursor, we selected a star and performed aperture photometry
  on that star ("`a`"). `Imexamine` outputted properties of the star such as
  position, flux and magnitude to the file *logfile*.

- This procedure was then repeated for the next image.

A.2.2 Image Shifting

The required shifting of the images in each grid was done interactively using two `IRAF` scripts.

The first script displayed each image in the grid using `imexamine`. A reference star which is visible in each frame was chosen. The coordinates of the star in the first frame was obtained using `imexamine`: the image was displayed, the cross–hairs are placed on the star, and the coordinates were calculated using a centroid algorithm and written to a log file. This procedure was repeated for the remaining images.

The second script used the recorded values to determine the shift for each image. Each frame was shifted, and a corresponding bad pixel map created, using commands similar to: `imshift` *input=image.imh xshift = 27.06 yshift = 31.84 output=image_sft.imh.*

A.2.3 `DAOPHOT` Options

A PSF model generally consists of two components: (i) an analytic function which models the core of the stars, and (ii) one or more look-up tables . The tables list the residuals of the analytic fit to the remaining annuli of the stars, and are used to improve the fit of the annuli. The *daopars* pset parameters decide the number of look-up tables and the type of analytical model selected.

function The type of analytical model(s) to be employed for the PSF. Possible models are: Gaussian, Moffat, Lorentzian, or Gaussian core with Lorentzian wings. A value of *auto* for this parameter causes `psf` to determine which model fits the data best (i.e., has the smallest χ_r^2 value). For our analysis, we chose a Gaussian function.

varorder Determines the number of the look-up table used. If *varorder* is set to -1, no look-up table is used. This is useful for severely undersampled data. A *varorder* of 0 results in a constant model, which creates only one look-up table. A variable model is created by selecting a *varorder* of 1 or

2. These models construct three and six look-up tables, respectively. This parameter was set to 0 for our data.

fitrad Determines the area where the analytical fit is applied. This should generally be set to the full-width at half-maximum (FWHM) of the selected model stars. We selected a *fitrad* value of 3.2 pixels initially for the fainter stars, and then 4 for the bright stars.

psfrad Sets the area where the empirical fit is applied. The brightest star of interest was selected. `Imexamine` was run to determine at what radius from the the centre of this star the flux from the star was indistinguishable from the noise. The distance (8 pixels) from this point to the centre of the star was selected as the value for *psfrad*.

A.2.4 `DAOPHOT` Procedure

The `DAOPHOT` parameters having been set to their correct values, a list of the stars of interest and their coordinates was created, either using `daofind` or `imexamine`. The commands then run to obtain the instrumental magnitudes of the selected stars were:

phot Performs automatic aperture photometry on each star.

pstselect Uses the output from `phot` to select possible PSF model stars.

psf Allows the user to interactively choose suitable PSF model stars from the candidates, and to create a PSF model. (We generally selected 3 or 4 model stars from a list of approximately 15.)

nstar Uses the PSF to fit the stars of interest, and check the accuracy of the model.

substar Subtracts the fitted stars from the original image. This image is then viewed to look for residuals left after the subtraction.

allstar Determines the magnitude of the selected stars.

A.3 Spectroscopy

A.3.1 `Apall`

This routine was used to extract the spectra from the raw images. `Apall` automatically distinguishes the spectrum of the star from the sky background and the noise, and traces the spectrum. The following parameters determine the extraction process:

format The format for the extracted spectra. The *multispec* format was chosen for our spectra.

references A list of images to select as aperture references. This parameter was set to the null string for the target spectra. For extracting an arc spectrum, it was set to the corresponding reference image name.

interactive Decides whether the task is run interactively or not. The target spectra were extracted interactively (*interactive = yes*), whereas the arc spectra were automatically extracted (*no*).

background Determines what type of background to subtract. No background was subtracted from our spectra using `apall` (*background = none*), as we subtracted the background manually.

saturation The saturation level of the detector.

readnoise The read out noise of the detector – this parameter was automatically read from the *RDNOISE* field of the image headers.

gain The photon gain of the detector – this was read by `IRAF` from the *GAIN* header field.

A.3.2 `Identify`

`Identify` was used to display an arc spectrum and match the spectral features with their corresponding wavelengths. It then computed a pixel to wavelength conversion function. The parameters modified from their default values for our spectra were:

coordlist Selects the coordinate list used to identify the arc lines. For our arcs, we chose the supplied *linelists$argon.dat*.

units The type of units to be used for the coordinates entered. Our data were given in *microns.*

fwidth The full-width at zero of the features in the arc spectrum. We determined this value to be 8 pixels.

function The function to be applied to fit the dispersion correction. We selected a cubic spline – *spline3.*

order The order of *function.* Our spline had order 3.

A.3.3 Reidentify

Rather than using `identify` on each individual arc, the `reidentify` task was run in order to apply the previous identification of the spectral features in the original arc to identify the features in successive arcs. The identification process is modified by changing the following parameters:

images A list of the images to be reidentified.

interactive Decides whether the task is run interactively or not.

shift The shift to apply to the user-specified coordinates for the arc features. This was set to *INDEF*, allowing `IRAF` to calculate any necessary shift.

search When *shift* is set to *INDEF*, this value specifies how `IRAF` calculates the shift. This was set to *INDEF*. `IRAF` therefore compared the line peaks in the spectra to determine the shift.

coordlist Again, the coordinate list *linelists$argon.dat* was selected.

A.3.4 Splot

`Splot` can be used to extract various properties interactively from a spectrum. Either a single spectrum, or a group of spectra can be examined. `Splot` was used in the following ways with our spectra:

- Having obtained a combined spectrum of our target GRO J1655–40, we smoothed this spectrum using the "`s`" cursor command. This implemented a boxcar smooth.

- We measured the equivalent width of a spectral feature as follows. First, we viewed the spectrum using `splot` and expanded the view of the spectrum to the area around the spectral line ("`a`" command). We then indicated the position of the feature using the "`e`" command, which then displayed the wavelength of the feature and the equivalent width. We loaded the next spectrum by typing "`g`", and repeated the procedure.

- The masking of a spectral feature was performed using the "`j`" command. The view of the spectrum was zoomed into the spectral feature, and the flux value was set to the continuum value. This new spectrum was then saved by typing "`i`".

Bibliography

Bailyn C. D., 1992, ApJ, 391, 298

Bailyn C. D., Jain R. K., Coppi P., Orosz J. A., 1998, ApJ, 499, 367

Bailyn C. D., Orosz J. A., Girard T. M., et al., 1995a, Nat, 374, 701

Bailyn C. D., Orosz J. A., McClintock J. E., Remillard R. A., 1995b, Nat, 378, 157

Barnes J., 1993, A Beginner's Guide to Using IRAF, IRAF Documentation, National Optical Astronomy Observatories, Arizona, US

Beer M. E., Podsiadlowski P., 2002, MNRAS, 331, 351

Bevington P. R., 1969, Data Reduction and Error Analysis for the Physical Sciences. McGraw-Hill, New York

Blair W. P., Raymond J. C., Dupree A. K., et al., 1984, ApJ, 278, 270

Bolton C. T., 1972, Nat, 235, 271

Brandt W. N., Podsiadlowski P., Sigurdsson S., 1995, MNRAS, 277, L35

Callanan P. J., 2001, private communication

Callanan P. J., Charles P. A., 1991, MNRAS, 249, 573

Callanan P. J., Garcia M. R., Filippenko A. V., McLean I., Teplitz H., 1996, ApJ, 470, L57

Cardelli J. A., Clayton G. C., Mathis J. S., 1989, ApJ, 345, 245

Carroll B. W., Ostlie D. A., 1996, An Introduction to Modern Astrophysics. Addison-Wesley, Reading, Massachusetts

Casares J., 2001, X-ray binaries and black hole candidates: a review of optical properties, in Lázaro F. C., Arévalo M. J. (eds.), Binary Stars: Selected Topics on Observations and Physical Processes. Springer-Verlag, Berlin, p. 277

Casares J., Charles P. A., Naylor T., 1992, Nat, 355, 614

Chaty S., Mirabel I. F., Goldoni P., et al., 2002, MNRAS, 331, 1065

Chevalier C., Ilovaisky S. A., van Paradijs J., Pedersen H., van der Klis M., 1989, A&A, 210, 114

Chitre D. M., Hartle J. B., 1976, ApJ, 207, 592

Curran P. A., 2001, Master's thesis, National University of Ireland, Cork, Ireland

Davis L. E., 1994, A Reference Guide to the IRAF/DAOPHOT Package, IRAF Documentation, National Optical Astronomy Observatories, Arizona, US

Elvis M., Page C. G., Pounds K. A., Ricketts M. J., Turner M. J. L., 1975, Nat, 257, 656

Fabian A. C., 1985, Pringle J. E., Wade R. A. (eds.), Interacting binary stars, Cambridge Astrophysics Series. Cambridge University Press, Cambridge, Ch. 2.3, p. 71

Froning C. S., Robinson E. L., 2001, AJ, 121, 2212

Giacconi R., Gursky H., Paolini F. R., Rossi B. B., 1962, Phys. Rev. Lett., 9, 439

Gray D. F., 1992, The observation and analysis of stellar photospheres (Second ed.). Cambridge University Press, Cambridge, Ch. 17, p. 368

Greene J., Bailyn C. D., Orosz J. A., 2001, ApJ, 554, 1290

Harmon A., 1996, private communication

Harmon B. A., Wilson C. A., Zhang S. N., et al., 1995, Nat, 374, 703

Harries J. R., McCracken K. G., Francey R. J., Fenton A. G., 1967, Nat, 215, 38

Hjellming R. M., Rupen M. P., 1995, Nat, 375, 464

Hynes R. I., Haswell C. A., Shrader C. R., et al., 1998, MNRAS, 300, 64

Israelian G., Rebolo R., Basri G., Casares J., Martin E. L., 1999, Nat, 401, 142

King A. R., Kolb U., Burderi L., 1996, ApJ, 464, L127

Kolb U., King A. R., Ritter H., Frank J., 1997, ApJ, 485, L33

Lewin W. H. G., van Paradijs J., van den Heuvel E. P. J. (eds.), 1995, X-ray Binaries, Cambridge Astrophysics Series No. 26. Cambridge University Press, Cambridge, MA

Liu Q. Z., van Paradijs J., van den Heuvel E. P. J., 2000, A&AS, 147, 25

Liu Q. Z., van Paradijs J., van den Heuvel E. P. J., 2001, A&A, 368, 1021

McClintock J. E., Remillard R. A., 1986, ApJ, 308, 110

Meyer-Hofmeister E., Meyer F., 2000, A&A, 355, 1073

Mirabel I. F., Mignani R., Rodrigues I., et al., 2002, A&A, 395, 595

Orosz J. A., Bailyn C. D., 1997, ApJ, 477, 876

Orosz J. A., Groot P. J., van der Klis M., et al., 2002, ApJ, 568, 845

Orosz J. A., Hauschildt P. H., 2000, A&A, 364, 265

Pringle J. E., 1985, Pringle J. E., Wade R. A. (eds.), Interacting binary stars, Cambridge Astrophysics Series. Cambridge University Press, Cambridge, Ch. 1, p. 1

Pringle J. E., Wade R. A. (eds.), 1985, Interacting binary stars, Cambridge Astrophysics Series. Cambridge University Press, Cambridge

Rhoades C. E., Jr., Ruffini R., 1974, Phys. Rev. Lett., 32, 324

Schroeder D. J., 1987, Astronomical Optics. Academic Press, Inc., New York, Ch. 16, p. 313

Shahbaz T., Bandyopadhyay R. M., Charles P. A., 1999, A&A, 346, 82

Shahbaz T., Naylor T., Charles P. A., 1993, MNRAS, 265, 655

Shahbaz T., Naylor T., Charles P. A., 1994, MNRAS, 268, 756

Shahbaz T., Naylor T., Charles P. A., 1997, MNRAS, 285, 607

Shahbaz T., Ringwald F. A., Bunn J. C., et al., 1994, MNRAS, 271, L10

Shahbaz T., Smale A. P., Naylor T., et al., 1996, MNRAS, 282, 1437

Shahbaz T., van der Hooft F., Casares J., Charles P. A., van Paradijs J., 1999, MNRAS, 306, 89

Shklovsky I. S., 1967, ApJ, 148, L1

Stetson P. B., 1987, PASP, 99, 191

Tanaka Y., Lewin W. H. G., 1995, Lewin W. H. G., van Paradijs J., van den Heuvel E. P. J. (eds.), X-ray Binaries, Cambridge Astrophysics Series No. 26. Cambridge University Press, Cambridge, MA, Ch. 3, p. 126

Tanaka Y., Shibazaki N., 1996, ARA&A, 34, 607

Tavani M., Fruchter A., Zhang S. N., et al., 1996, ApJ, 473, L103

Tingay S. J., Jauncey D. L., Preston R. A., et al., 1995, Nat, 374, 141

van der Hooft F., Heemskerk M. H. M., Alberts F., van Paradijs J., 1998, A&A, 329, 538

van Paradijs J., 1995, Lewin W. H. G., van Paradijs J., van den Heuvel E. P. J. (eds.), X-ray Binaries, Cambridge Astrophysics Series No. 26. Cambridge University Press, Cambridge, MA, Ch. 14, p. 536

van Paradijs J., 1998, Neutron Stars and Black Holes in X-Ray Binaries, in NATO ASIC Proc. 515: The Many Faces of Neutron Stars., p. 279

van Paradijs J., McClintock J. E., 1995, Lewin W. H. G., van Paradijs J., van den Heuvel E. P. J. (eds.), X-ray Binaries, Cambridge Astrophysics Series No. 26. Cambridge University Press, Cambridge, MA, Ch. 2, p. 58

Wallace L., Hinkle K., 1997, ApJS, 111, 445

Webster B. L., Murdin P., 1972, Nat, 235, 37

White N. E., Nagase F., Parmar A. N., 1995, Lewin W. H. G., van Paradijs J., van den Heuvel E. P. J. (eds.), X-ray Binaries, Cambridge Astrophysics Series No. 26. Cambridge University Press, Cambridge, MA, Ch. 1, p. 1

Wilson R. E., Devinney E. J., 1971, ApJ, 166, 605

Zhang S. N., Ebisawa K., Sunyaev R., et al., 1997, ApJ, 479, 381

Zhang S. N., Wilson C. A., Harmon B. A., et al., 1994, IAU Circ., 6046, 1